An experimental study of the low-lying quadrupole excitations of ^{212}Po

by
Diana Kocheva

Dissertation for acquiring the Doctor of Philosophy Degree
in Physics
Specialization "Nuclear Physics"
University of Sofia St. Kliment Ohridski
2018

Abstract

The present study is focused on the properties of the low-lying quadrupole valence-shell excitations in ^{212}Po, a nucleus that has two valence protons and two valence neutrons with respect to the double-magic nucleus ^{208}Pb. The lifetimes of the first three 2^+ states of ^{212}Po, were measured by means of in-beam γ-ray spectroscopy of excited states which were populated in a ^{208}Pb(^{12}C,^{8}Be)^{212}Po transfer reaction. The lifetimes of the 2_2^+ and 2_3^+ excited states, candidates for the one-phonon mixed-symmetry state, were determined by utilizing the Doppler shift attenuation method. The resulting absolute transition strengths reveal that the 2_2^+ state of ^{212}Po is of predominantly isovector nature. This represents the first identification of a low-lying isovector state in a nucleus in the vicinity of the double-magic nucleus ^{208}Pb. The experimental data also reveals a weakened quadrupole collectivity in these non-yrast states. These experimental results are in qualitative agreement with a single-j shell model calculation, which, together with the observed lack of quadrupole collectivity, indicates that the isovector nature of this low-lying state is a generic property originating from the two-fluid quantum nature of the leading single-particle valence-shell configurations.

The lack of collectivity in the structure of the 2^+ isovector state of ^{212}Po is a peculiar feature which has not been observed so far in isovector states in other mass regions. To investigate further the degree of quadrupole collectivity in ^{212}Po the lifetime of the 2_1^+ state has been measured by means of the Recoil Distance Doppler Shift (RDDS) method. The derived absolute $B(E2)$ value of 2.6(3) W.u. indicates a very low collectivity in the structure of this state. Qualitatively, a low transition strength from this state can be expected within the framework of the single-j shell model since its wave function is neutron dominated. However, it is demonstrated that a consistent description of the properties of the $2_1^+ - 4_1^+ - 6_1^+ - 8_1^+$ sequence in ^{212}Po cannot be achieved by shell-model calculations. The problem appears to originate from the properties of the seniority-2 configurations in ^{210}Pb and ^{210}Po. The question how these seniority-2 states form the low-lying states of ^{212}Po represents a challenge to the contemporary microscopic models.

Contents

Chapter 1

Introduction

1.1 Theoretical background

Since the discovery of the atomic nucleus (more than 100 years ago) nuclear physics has been an active field of research. It is known that the nucleus is a very complex system - a collection of species ranging from hydrogen to the actinides and displaying a rich variety of phenomena. The atomic nucleus can contain up to a couple of hundred individual protons and neutrons that orbit relative to one another and interact via the nuclear and Coulomb forces.

From empirical point of view, the collective nuclei can be classified by using various experimental observables, *e.g.*, the energies and transition strengths of excited nuclear states. One well-known example is the excitation energies of the 2_1^+ and 4_1^+ states in nuclei with even numbers of protons and neutrons. The ratio of these energies, $R_{4/2} = E(4_1^+)/E(2_1^+)$, exhibits a very uniform behaviour as a function of the distance from the nuclear magic numbers [1]. In other words, this ratio is an indication for the degree of collectivity in nuclei. The overview of the $R_{4/2}$ values across the chart of nuclei is shown in Fig. 1.1.

The complexity of the nuclear system requires the using of different models along the nuclear chart in order to interpret the different structures observed experimentally. In order to describe very light nuclei and those that are very near to closed shells the *Shell model* [3,4] is widely used. This model is based on a microscopic approach considering individual nucleons. In cases when the nuclei are far from closed shells, the use of the shell model becomes very difficult since the size of the matrices in which the residual interaction has to be diagonalized becomes prohibitively large. At the same time the strong proton-neutron interaction leads to the onset of collectivity [1,5]. For these nuclei a macroscopic approach is used. The *Liquid-Drop model*, in the version of Bohr and Mottelson [5] describes the nucleus as a quantum fluid, being able to perform vibrations and rotations, while also changing its overall shape. This model describes the collective motions of the nucleus. Another approach for describing collective excitations in nuclei is the *Interacting Boson Model* which was proposed by F. Iachello and A. Arima [6]. The basic idea is to assume that the valence fermions (protons and neutrons) couple in pairs and that the low-lying collective excitations of medium and heavy nuclei can be described in terms of the energies and interactions of such pairs.
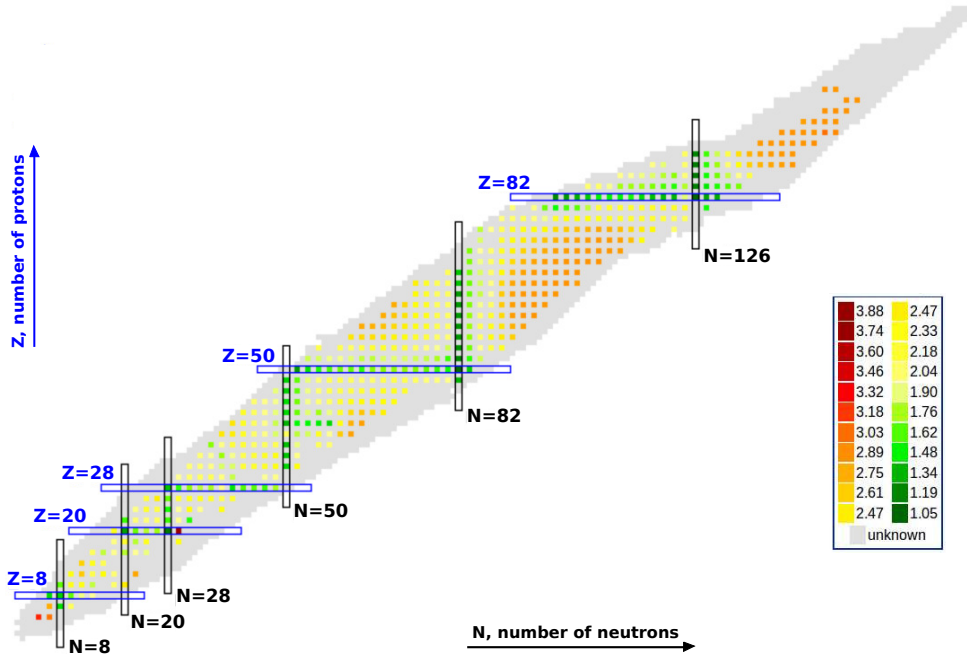
Figure 1.1: Color-coded illustration of the ratio $R_{4/2} = E(4_1^+)/E(2_1^+)$ for the even-even nuclei across the entire nuclear chart [2]. The colors code indicates the shape and behaviour of the nuclei, *i.e.* for values from < 2 (green, spherical shape) to 3.33 (red, well deformed). The onset of deformation when moving from closed shells to midshell regions is apparent.

A short overview of all of the above-mentioned theoretical models will be given in the subsequent chapter in order to provide the reader with the theoretical background used for the interpretation of the experimental results in the present study. This is achieved by a compilation of the available literature. The original contribution by the author is summarized in chapters 3, 4, 5 and 6, where the data analysis and the interpretation of the results are presented.

1.2 Scientific motivation for studying the nucleus ^{212}Po

There are two fundamental concepts for describing the nuclear excitations - single-particle and collective motions. Understanding nuclear structure in terms of both regimes is one of the challenges of nuclear physics. In this regard, properties of open-shell nuclei in the immediate vicinity of double-magic cores are of particular importance due to the fact that such nuclei can often be understood well within the framework of the shell models and at the same time their valence particles can induce the onset of collective behaviour. In this picture the low-energy excitations of semi-magic nuclei can be considered as single-particle excitations resulting from the recoupling of the valence protons (or neutrons). Such states will preserve the 'seniority' v quantum number [7] which is the number of unpaired nucleons. In open-shell nuclei that are close to shell closures the proton-neutron

interaction induces collectivity. However, in heavy nuclei where the proton and neutron energy spaces are well separated, it can be expected that the seniority features remain preserved to a large extend [8]. With increasing the number of valence particles the seniority picture breaks down and evolves towards collective (vibrational) mode.

The nucleus ^{212}Po has two valence protons and two valence neutrons with respect to the double-magic core ^{208}Pb, thus providing a good testing ground for studying the beginning of the evolution from single-particle to collective motion in the mass A $\approx$ 208 region. In the microscopic approach, the valence neutrons of ^{212}Po are in the $2g_{9/2}$ shell and the protons are in the $1h_{9/2}$ shell. It was suggested by Auerbach and Talmi [9] that the yrast sequence $2_1^+ - 4_1^+ - 6_1^+ - 8_1^+$ of ^{212}Po follows a seniority-like energy pattern resulting in an isomeric 8_1^+ state. The isomeric nature of the 8_1^+ state has later been confirmed in a series of α- and γ-spectroscopy studies [10]. A complete level scheme of ^{212}Po deduced from a $\gamma - \gamma$ coincidence experiment has been reported later on by Poletti $et\ al.$ [11] together with the lifetimes of the 6_1^+ and the 8_1^+ states. This level scheme has undergone numerous checks [12] and can be considered as well established. However, the crucial experimental information, namely the lifetimes of the 2_1^+ and the 4_1^+ states is still missing [12].

The properties of nuclei with two valence protons and two valence neutrons also reflect the two-fluid nature of the nuclear matter. It is expected that such nuclei will have well pronounced low-lying 2^+ isovector states [13]. In these states the valence protons and neutrons move out of phase. The properties of these states are sensitive to the isovector part of the proton-neutron interaction. The low-lying isovector states in open-shell vibrational nuclei are also known as mixed-symmetry states (MSSs) which are defined in the framework of the Interacting Boson Model-2 (IBM-2) [6]. It is known that the mixed-symmetry states can be identified experimentally by their strong isovector $M1$ decay to the low-lying fully-symmetric states (FSSs) [15,24]. The best examples of MSSs of stable nuclei are found in the mass A $\approx$ 90 region [15]. In the last decade a large number of MSSs has been identified in the mass A $\approx$ 130 region, $i.e.$ the mass region around the double-magic nucleus ^{132}Sn [16–21].

It has to be noted, however, that the MSSs are considered as weakly collective quadrupole states. It is not clear how they will appear in non-collective nuclei, $i.e.$ it is not clear how strong is the connection between the isovector nature of these states and the quadrupole collectivity of the valence-shell configuration. Apparently, for better understanding for the formation of the low-lying isovector excitations, more cases of one-phonon MSSs in the vicinity of double-magic nuclei have to be identified and quantitatively studied. However, nuclei in the vicinities of double-magic shell closures in which the one-phonon $2_{1,ms}^+$ can be studied experimentally by conventional methods are scarce. For instance, in the mass region around the double-magic nucleus ^{132}Sn, all such nuclei are neutron-rich and radioactive. The situation around the double-magic nucleus ^{208}Pb is somewhat different because the nucleus ^{212}Po is experimentally accessible via α-transfer reactions [22]. Moreover, there are two potential candidates for the one-phonon MSS in ^{212}Po due to the fact that its $2_{2,3}^+$ states decay predominantly to the 2_1^+ state [12] as both transitions have a well pronounced $M1$ character with multi-

pole mixing ratios of $+0.09(3)$ and $+0.65(50)$ [23], respectively. The only missing piece of experimental information is the large absolute $M1$ transition strengths corresponding to short lifetimes of these levels.

The aim of the present study is to investigate experimentally the properties of low-lying states of ^{212}Po, both the isoscalar and isovector ones, in order to illuminate the transition from single-particle (seniority type) to collective mode. It will be shown that the lifetime of the first isoscalar 2^+ state is of particular importance. Surprisingly, the quadrupole strength in ^{212}Po is even lower than the one expected from the seniority scheme. This feature appears also in the properties of the $2^+_{1,ms}$ of ^{212}Po which in fact is the first isovector state experimentally identified around ^{208}Pb. The identification of this state and its properties can be considered as a starting point of the present study. The final results clearly indicate a peculiarity that cannot be understood in the framework of any of the contemporary theoretical models. Apparently, the quadrupole collectivity around ^{208}Pb develops in a more strenuous way as the single-particle character remains more robust than expected.

Chapter 2

Low-lying quadrupole states in low collective even-even nuclei

This chapter briefly introduces some of the basic concepts of the models used for describing the low-lying quadrupole excitations in low-collective even-even nuclei. In the first section a brief overview of the description of nuclear structure as resulting from both the single-particle motion and the residual interactions is given. The basic idea of the seniority scheme is presented. The shell model offers a good description for nuclei close to magic cores. When adding or removing nucleons from a closed shell configurations, the valence nucleons in the open shell start to interact thus leading to collective motion. In these cases the shell model is not applicable or at least it becomes computationally challenging. For these nuclei another approach for describing their structure in terms of collective motions is used. The most relevant concepts here are shortly introduced in section 2.1.3. The last part of this chapter introduces the Interacting Boson Model (IBM) which originates from a truncation of the nuclear shell model space and, yet, is capable of describing collectivity of nuclei across the nuclear chart. One key feature of the IBM is its algebraic structure that distinguishes it from the previously discussed models.

2.1 Description of low-lying states in the framework of single-particle and collective models

2.1.1 Shell model

The nuclear shell model was developed independently by Maria Goeppert-Mayer [3] and Haxel, Jensen, and Suess [4]. Its invention was successful, because it was capable of explaining the increased stability of nuclei consisting of the particular magic numbers of protons and neutrons: 2, 8, 20, 28, 50, 82, and 126. The magic numbers correspond to closed shells in nuclei analogously to the filling of electron shells in atoms.

The starting point for microscopic description of nuclear structure is the interaction between the nucleons. Every nucleon, which is part of an atomic nucleus, possesses a particular kinetic energy and is subject to interactions with other

nucleons. This force between nucleons is, for simplicity, assumed to be of 2-body nature. The Hamiltonian can then be written as

$$H = T + V = \sum_{i=1}^{A} \frac{\vec{p_i}^2}{2m_i} + \sum_{i>k=1}^{A} V_{ik}(\vec{r_i} - \vec{r_k}) \tag{2.1}$$

The Hamiltonian has 3A position and momentum coordinates and it is extremely difficult to be solved. The fundamental idea behind the shell model is that in first approximation the nucleons can be considered as independent particles moving in a central potential generated by the interaction between them. The original Hamiltonian is modified by introduction of a 1-body potential $U_i(r_i)$:

$$H = \underbrace{\sum_{i=1}^{A} \left[\frac{\vec{p_i}^2}{2m_i} + U_i(r_i) \right]}_{\equiv H_0} + \underbrace{\sum_{i>k=1}^{A} V_{ik}(\vec{r_i} - \vec{r_k}) + \sum_{i=1}^{A} U_i(r_i)}_{\equiv H_{res}} \tag{2.2}$$

The contribution of the residual interaction H_{res} is assumed to be small. In first approximation it can be neglected, which is a good approximation for nuclei having one nucleon outside closed shell. The residual interaction gives rise to collective excitations. Due to the short-range character of the nucleon-nucleon interaction, the potential $U(r)$ can be approximated by the Harmonic Oscillator (HO),

$$U(\vec{r}) = \frac{1}{2}m\omega^2\vec{r^2} \tag{2.3}$$

The energy levels of the harmonic oscillator potential are shown on the left in Fig. 2.1. This potential leads to magic numbers: 2, 8, 20, 40, 70, 112. We note that the first three of these indeed reproduce the known magic numbers but the last ones do not. Therefore, while the harmonic oscillator potential is a reasonable first order approximation to the effective nuclear potential, it must be modified to be useful [1].

Let us consider a relatively heavy nucleus with size significantly larger than the range R_N of the nuclear force. Then, as long as a given nucleon lies inside the nuclear surface at a distance greater than R_N, it should be surrounded rather uniformly by nucleons on all sides. It is thus screened from the asymmetric distribution that appears at the boundary. Therefore, it should experience no net force. In other words, the central part of the nuclear potential should be approximately constant. This can be achieved by changing the potential, but this will lead to more complicated solutions. Another possibility is to add an attractive term in l^2 to the harmonic oscillator potential. The effects of an l^2 term increase with the orbital angular momentum of the particle. Therefore high angular momentum particles feel stronger attractive interaction that lowers their energies. However, these are the particles that, because of the centrifugal force, spend most of the time at larger radii. Therefore, the addition of an l^2 term is equivalent to a more constant interior potential. The relation of the single-particle levels produced by a harmonic oscillator potential, along with an l^2 term is presented in the middle panel of Fig. 2.1. It is shown how the degeneracy of the harmonic oscillator
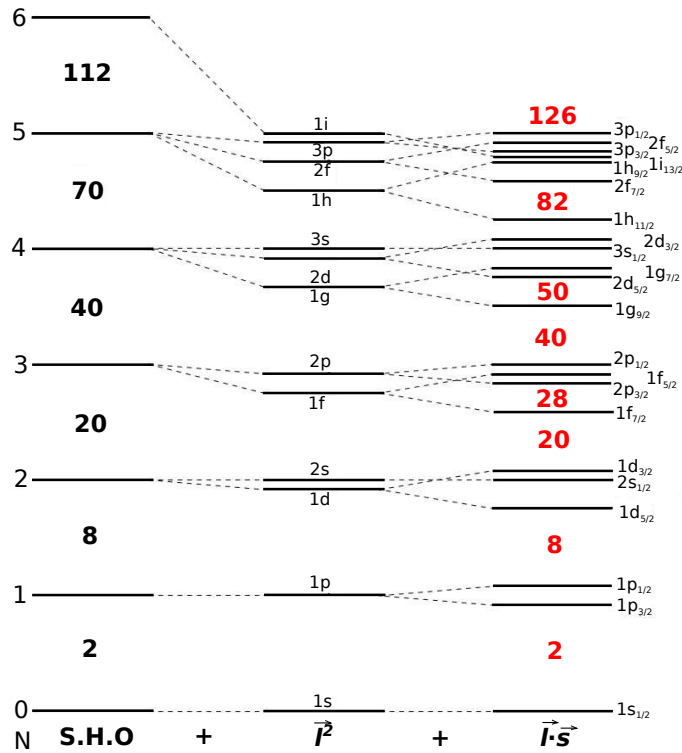
Figure 2.1: Qualitative illustration of the orbitals emerging in the nuclear shell model, adapted from [1].

levels is lifted as high angular momentum levels are brought down in energy [1]. This is an improvement in comparison to the sole harmonic oscillator potential, but, nevertheless, does not generate the known magic numbers. Coupling the orbital angular momentum l and the intrinsic nucleon spin s yields another term, modifying the potential for a nucleon, depending on whether the spin is aligned parallel or antiparallel to the angular momentum. This leads to lowering of levels with $j = l + s$ and raising of levels with $j = l - s$.

The complete single-particle potential then is given by

$$U(\vec{r}) = \frac{1}{2}m\omega^2\vec{r^2} - V_l\vec{l^2} - V_{ls}\vec{l}\cdot\vec{s} \tag{2.4}$$

Inserting this central potential into the Hamiltonian H_0 of Eq. 2.2 yields the solution illustrated on the right side of Fig. 2.1. The orbits are labeled with the quantum numbers nl_j , where n is the radial quantum number, l is the orbital angular momentum, and j is the total angular momentum $j = l \pm 1/2$. According to the Pauli principle each orbit can be populated by $2j + 1$ nucleons. Filling the orbits consecutively results in large energetic gaps for nucleon numbers that correspond to the empirical magic numbers. This reproduces all the known magic numbers.

As a consequence of the Pauli principle, the $2j + 1$ nucleons of a completely filled orbit couple to total angular momentum $J = 0$. Hence, the properties of nuclei are determined by the nucleons in partially filled orbits, so-called *valence nucleons*. They are, to first order, subject to the residual interaction, only. Va-

13

lence nucleons of the same kind in the same orbit can couple to different angular momenta J, whose degeneracy is removed by the residual interaction between them.

An example of such a residual interaction is the δ interaction

$$V_{res} = -V_0\delta(\vec{r}_1 - \vec{r}_2) \tag{2.5}$$

which models the short-range attractive part of the nuclear force. The δ interaction is maximal for two nucleons with maximum spatial overlap of their wave functions.

Another important interaction in the case of more than one valence nucleon is the pairing interaction. The motivation is similar to that for the δ interaction - the pairing interaction is only effective when the particles have high spatial overlaps. Formally, one can define the pairing interaction by [1]

$$\langle j_1 j_2 J | V_{pair} | j_3 j_4 J' \rangle = -G\sqrt{(j_1 + 1/2)(j_3 + 1/2)}\delta_{j_1 j_2}\delta_{j_3 j_4}\delta_{J0J0'} \tag{2.6}$$

where G gives the strength of the interaction. Note that this interaction is attractive and, by definition, only effective for 0^+ states of identical nucleons in equivalent orbits. However, it allows nondiagonal scatterings, $\langle j_1^2 0^+ | V_{pair} | j_3^2 0^+ \rangle$, in which a pair of particles switches to another orbit as a pair. This feature is critical to the build-up of pairing correlations and the so-called pairing gap in even-even nuclei.

Both the δ function force and the pairing force are intended to represent the short-range component of the nuclear interaction. However, the residual interaction also contains a long-range component that is crucial in producing collective properties and nonspherical nuclei. Usually, this component is presented by the so-called quadrupole interaction. The combination of the quadrupole and pairing forces, the so-called pairing plus quadrupole interaction, has been perhaps the most widely used for modelling the nuclear interactions in heavy nuclei [1].

The popularity of the pairing interaction, or of any other that reproduces the low energy of $J = 0$ coupled pairs of nucleons, clearly lies in the fact that all even-even nuclei have 0^+ ground states.

2.1.2 Seniority scheme

The tendency of particles to pair to $J = 0^+$ leads to a scheme in which this property is explicitly recognized and exploited. Considering j^n configuration it is interesting to see what the smallest value for n is that can produce a given J value. This value can be denoted by ν and in this case it is clear that there can be no particles coupled in pairs to $J = 0$ in the configuration $j^\nu J$ ($J \neq 0$). Otherwise, a $j^{\nu-2}$ configuration would have a spin J. Such a state is said to have seniority ν. From a configuration $j^{\nu+2}$ a state of the same spin J can be made by coupling one pair of particles to $J = 0^+$. For this state is also said to have seniority ν. Physically, ν is simply the number of unpaired particles in a state with angular momentum J in the configuration j^n. The number of paired particles is $(n - \nu)$ and the number of such pairs is $(n - \nu)/2$. For $\nu = 0$, all particles are paired and $J = 0$ [1].

The seniority concept is very important due to the fact that it leads to many simple powerful results under quite general conditions. For example, various interactions and matrix elements can be classified in terms of whether or not they conserve seniority. Even more important is that many realistic residual interactions conserve seniority, so this scheme gives reasonable predictions for actual nuclei. It is impossible within the scope of this thesis to derive all the results of the seniority scheme without adding an undesirable and unnecessary complexity. In the following paragraphs the most important properties of the seniority regime are summarized.
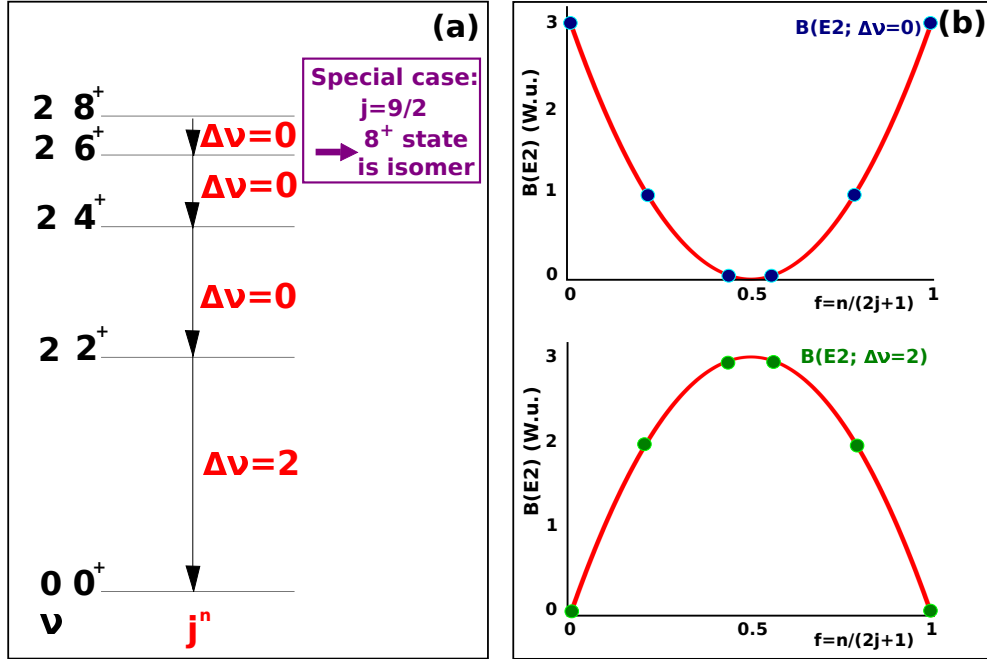

Figure 2.2: (a) Illustration of the low-lying states following seniority-like energy pattern; (b) $B(E2)$ values for $J \rightarrow J-2$ transitions for seniority conserving (upper panel) and seniority changing (bottom panel) transitions as a function of fractional filling.

The appealing feature of the seniority scheme is that matrix elements between configurations in j^n can be reduced to those in j^ν. Thus, all energy differences of seniority $\nu = 0$ and $\nu = 2$ states in the n-particle configuration are identical to those in the two-particle system and are independent of n. This result is crucial because its absence would make impossible the application of the shell model in a simple way to nuclei other than those within one or two nucleons outside the closed shells.

Considering nuclei with two particles (or holes) of the same type (protons or neutrons) outside the double-magic core in a single-particle orbit j, the levels up to spin $J = 2j - 1$ can be denoted by the wave function $|j^2 \nu J\rangle$. The 0^+ ground state must have the two particles coupled to spin zero, while for the $2^+, 4^+, \ldots, (2j - 1)$ states the pair is broken. The seniority classification leads to a distinction between $E2$ transitions from one of these levels to another: the $2_1^+ \rightarrow 0_1^+$ transition changes seniority ($\Delta\nu = 2$) while transitions for higher J

15

values are seniority conserving ($\Delta\nu = 0$). In Fig. 2.2(a) an illustration of the low-lying states following the seniority pattern is represented. For a short range residual interaction the spacings between the $0^+, 2^+, 4^+, \ldots, (2j-1)$ states decrease monotonically for a j^n configuration [26]. The low energy of the $(2j-1) \rightarrow (2j-3)$ transition often makes the $(2j-1)$ state isomeric [26]. In Fig. 2.2(a) a special case is illustrated - when the valence nucleons occupy $j = 9/2$ single-particle orbit. This example has been chosen because the lowest-lying orbital in the valence space above the double-magic core of ^{208}Pb are the $2g_{9/2}$ shell (for neutrons) and $1h_{9/2}$ shell (for protons). In this case, the 8^+ state is expected to be isomer which is confirmed by the available experimental data [12].

It is interesting to see the behaviour of the $B(E2)$ values for seniority conserving and seniority nonconserving transitions. The expressions for the $E2$ transition matrix elements for both types of transitions are well known in the seniority scheme and their form can be found in Refs. [1, 26]. However, we choose to use a more illustrative approach. In Fig. 2.2(b) the calculated $B(E2)$ values for $J \rightarrow J - 2$ transitions for seniority conserving and seniority changing transitions are presented as a function of the fractional filling $f = n/(2j + 1)$ of the j shell [26]. The $B(E2)$ values of the seniority conserving transitions follow a parabolic trend with their minimum being at the mid-j shell. The $B(E2)$ values of the seniority changing transitions follow completely different trend. They reach their maximum at the mid-j shell [26, 27].

We would like to emphasize that the parabolic trend for seniority conserving transition is in complete contrast to the behaviour of these transitions in collective nuclei, where the $B(E2; J \rightarrow J-2; J > 2)$ values increase to midshell, replicating the behaviour of the $B(E2; 2_1^+ \rightarrow 0_1^+)$ value in the seniority scheme. This is just another example for the importance of the $B(E2)$ strengths as experimental fingerprints for the onset of nuclear collectivity. Moreover, they give valuable insights into the nature of nuclear collectivity and its evolution with N and Z. In almost all even-even nuclei, $B(E2)$ values connecting the lowest yrast states behave in a simple way, increasing both with increasing valence nucleons and spin [26].

2.1.3 Collective motion

While the shell model offers a good description of nuclear structure for nuclei closed to the magic cores, when adding or removing protons/neutrons from a closed-shell configurations, the particles/holes in the open shell start to interact and the nuclei start to behave as collective ones. A very figurative idea proposed by Bohr and Mottelson [5] is based on the assumption that the collective excitations are related to changes of nuclear shape, *i.e.* the nucleus is considered as a quantum fluid with a certain shape. Nuclear excitations are described in this model as arising from changes in the shape (vibrations) or changes of the orientation of non-spherical shape (rotations). Near closed shells, this liquid takes a spherical shape and can be excited to perform oscillations around this equilibrium shape (the nucleus vibrates), while in mid-shell regions the shape is deformed, which allows the nucleus to undergo rotational motion. Within the scope of the present thesis we are interested only into nuclei near closed shells, i.e. vibrational

ones.

The nuclear shape is mathematically described by parametrizing the nuclear surface in terms of an expansion in spherical harmonics $Y_{\lambda\mu}$

$$R(\theta, \phi, t) = R_0 \left(1 + \sum_{\lambda=0}^{\infty} \sum_{\mu=-\lambda}^{\lambda} \alpha_{\lambda\mu}(t) Y_{\lambda\mu}(\theta, \phi) \right) \tag{2.7}$$

In this expansion the term with $\lambda = 0$ can be neglected because it describes a nucleus that changes its volume while keeping its basic spherical shape [1]. This is the so-called *breathing mode* and might occur at very high energies. It can be neglected for the description of the low-lying collective states of the nucleus. The value of $\lambda = 1$ can also be neglected. It corresponds to a translation of the nucleus as a whole, which does not affect its internal structure. The higher values of $\lambda = 2, 3, \ldots$ correspond to quadrupole, octupole, etc. vibrations of the surface. Quadrupole modes are the lowest order ones at which collective excitations arise. In a geometrical picture this mode corresponds to oscillations between a flattening or an elongation of the nucleus followed by restoration of the spherical shape. In the following lines, the discussion will focus on quadrupole collectivity ($\lambda = 2$). For that class of excitations $\alpha_{\lambda=2,\mu}$ vanish, for odd μ, leaving α_{22}, α_{20} and α_{2-2} as unique collective degrees of freedom.

The Hamiltonian describing a quadrupole vibration can be written as [1]

$$H = T + V = \frac{1}{2} B \sum_{\mu} \left| \frac{\mathrm{d}\alpha_{2\mu}}{\mathrm{d}t} \right|^2 + \frac{1}{2} C \sum_{\mu} |\alpha_{2\mu}|^2 \tag{2.8}$$

where B plays the role of a mass parameter and C is a restoring force. Differentiating H, which is a constant of motion, gives

$$B \frac{\mathrm{d}^2 \alpha_{2\mu}}{\mathrm{d}t^2} + C \alpha_{2\mu} = 0. \tag{2.9}$$

This is identical in form to the differential equation of motion of a harmonic oscillator and hence we obtain the solution that (each of the) $\alpha_{2\mu}$ undergoes oscillations with frequency

$$\omega = \sqrt{C/B} \tag{2.10}$$

and vibrational energy $\hbar\omega$. Therefore, analogously to oscillations in rigid bodies, excitations of a vibrational nucleus can be deemed as phonons with angular momentum λ and parity $(-1)^\lambda$, i.e. quadrupole phonons with positive parity $J^\pi = 2^+$ in the case of quadrupole excitations $\lambda = 2$.

The allowed angular momenta for coupling of N phonons can be derived in the m-scheme [1]. The essential difference between the use of the m-scheme for phonon excitations and for single-particle excitations is the recognition that phonons, having integer spins, behave as bosons. Therefore, they are not affected by the Pauli principle. This means that all combinations of m states are allowed. This results in a triplet of $0^+, 2^+, 4^+$ states for two-phonon excitations and a quintuplet $0^+, 2^+, 3^+, 4^+, 6^+$ for three-phonon excitations. In practice, the states of a multi-phonon excitation are not exactly degenerate but form multiplets of

close-lying levels due to the residual interaction between the phonons that breaks the degeneracy of the multiplets, leading to small shifts in energy for the excited states, depending on the total angular momentum. For two phonon excitations, the value of $R_{4/2} = E(2_1^+)/E(4_1^+)$ is expected to be 2.2, which in fact is observed in collective nuclei near closed shells.

The excitation and decay of excited nuclear states, i.e. creation and destruction of such phonons, can be given in second quantization using quadrupole phonon creation and destruction operators $\mathbf{b}^\dagger$ and $\mathbf{b}$, defined via

$$\mathbf{b}|n_b\rangle = \sqrt{n_b}|n_b - 1\rangle \tag{2.11}$$

$$\mathbf{b}^\dagger|n_b\rangle = \sqrt{n_b + 1}|n_b + 1\rangle \tag{2.12}$$

where $|n_b\rangle$ is a state with n_b bosons. Therefore, excited N-phonon states can be constructed from the ground state $|0\rangle$ by successively applying the creation operator:

$$|N_{\mathrm{ph}}\rangle = (\mathbf{b}^\dagger)^N|0\rangle. \tag{2.13}$$

In the next section $\mathbf{b}$ will refer to either s or d bosons within the IBM framework.

2.2 Mixed-symmetry states (MSSs)

The quadrupole-collective isovector valence-shell excitations [28], the so-called mixed-symmetry states (MSSs) [6, 29], represent a unique quantum laboratory in which the balance and interplay between nuclear collectivity, shell structures, and isospin degree of freedom can be studied. States with proton-neutron mixed symmetry have been defined [29] in the framework of the interacting boson model with proton-neutron degree of freedom (IBM-2).

The Interacting Boson Model (IBM) is rooted in the spherical shell model [30], which is the fundamental model for describing properties of nuclei, but also has properties similar, and in many cases identical, to the collective model of Bohr and Mottelson [5]. Therefore, IBM can be used as an algebraic model describing low-energy collective excitations of atomic nuclei. The basic idea is, analog to the vibrational model of Bohr and Mottelson, to couple valence nucleons pairwise to bosons, thus drastically reducing the number of degrees of freedom.

There are several versions of the IBM depending on their degrees of freedom. The IBM in its original form (IBM-1 or sd-IBM-1) describes low-lying quadrupole-collective states with positive parity in medium and heavy even-even nuclei. In the IBM-1, protons and neutrons are not distinguished. This distinction is introduced in IBM-2 [29]. The extended IBM-3,4 version includes isospin degrees of freedom and allows one to treat light nuclei where protons and neutrons occupy the same single-particle orbits. There are other versions of the IBM - IBMF, sdf-IBM, sdg-IBM etc., which are outside the scope of the present discussion.

Since the results in the present study are related only to the IBM-2, we will briefly introduce this version of IBM in order to define its main experimental features. This presentation follows the book of Iachello and Arima [6] where the

complete formulation of the IBM can be found.

2.2.1 IBM-2 - the model describing the mixed-symmetry states

The basic approximating assumption of the IBM is that collective excitations can be described by bosons. These bosons can be of two types, s and d, having angular momentum of either L=$0\hbar$ or L=$2\hbar$, respectively. Both bosons have positive parity. The number of bosons is determined by the number of nucleon (or hole) pairs that are outside of a closed shell. The total number of bosons N in the IBM is conserved. The algebraic group that preserves this symmetry is U(6). In addition, for applications to atomic nuclei the chain of algebras have to contain the subalgebra O(3) since it is needed for states to have a representation of the rotation group. In other words, O(3) is required for states to have a good angular momentum quantum number. There are three unique reduction chains of the irreducible representations from U(6) to O(3). These three chains correspond exactly to the three types of collective excitations as is shown below:

$$\text{Chain 1} - \text{U(5): U(6)} \supset \text{U(5)} \supset \text{O(5)} \supset \text{O(3)} - \text{vibrational}$$
$$\text{Chain 2} - \text{SU(3): U(6)} \supset \text{SU(3)} \supset \text{O(3)} - \text{rotational}$$
$$\text{Chain 3} - \text{O(6): U(6)} \supset \text{O(6)} \supset \text{O(5)} \supset \text{O(3)} - \gamma\text{-soft}$$

All possible quadrupole collective excitations are enclosed between these three limits/symmetries which form the so-called symmetry triangle of IBM, also known as the Casten triangle [1] (see Fig. 2.3).
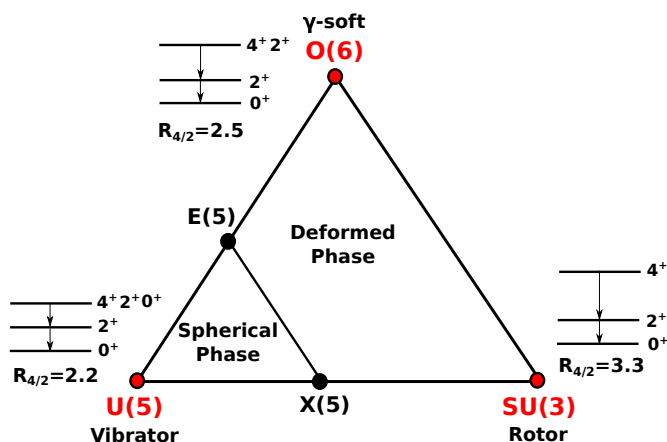

Figure 2.3: The symmetry triangle of IBM. The three limits of the vibrator, rotor and γ-soft shape (together with their algebraic group) are represented by the vertices while the legs of the triangle denote the corresponding transition regions. The typical energy pattern for these three nuclear shapes are represented as well.

The Interacting Boson Model-2 has been introduced as an extension to the IBM-1, which is necessary in order to account for the proton-neutron interaction. The proton and neutron bosons are interpreted as correlated pairs of valence protons and neutrons, respectively. Denoting the bosons by $b_{\rho,l,m}$ where ρ is the proton/neutron label, l is the angular momentum and m its magnetic substate,

the creation and annihilation operators fulfill the following commutation relations:

$$[b_{\rho,l,m}, b^{\dagger}_{\rho',l',m'}] = \delta_{\rho\rho'}\delta_{ll'}\delta_{mm'}$$

$$[b_{\rho,l,m}, b_{\rho',l',m'}] = [b^{\dagger}_{\rho,l,m}, b^{\dagger}_{\rho',l',m'}] = 0$$

The IBM-2 Hamiltonian can be written as a sum of three terms

$$H = H_\pi + H_\nu + V_{\pi\nu} \tag{2.14}$$

The terms H_π and H_ν are, in fact, the IBM-1 Hamiltonians for protons and neutrons, respectively. The difference between the IBM-1 and IBM-2 Hamiltonians is due to the presence of the third term $V_{\pi\nu}$ which is given by

$$V_{\pi\nu} = \sum_{\alpha\beta\gamma\delta} = w_{\alpha\beta\gamma\delta} b^{\dagger}_{\pi,\alpha} b_{\pi,\beta} b^{\dagger}_{\nu,\gamma} b_{\nu,\delta} + \cdots \tag{2.15}$$

This $V_{\pi\nu}$ conserves separately the number of proton and neutron bosons [6]. The underlying algebra of the IBM-2 is $U_\pi(6) \times U_\nu(6)$ with the subgroup $U_{\pi+\nu}(6)$ derived by adding the generators of the $U_\pi(6)$ and $U_\nu(6)$. Analogously to the reduction chains in IBM-1, one finds such chains for IBM-2, leading to the dynamical symmetries $U_{\pi+\nu}(5)$, $SU_{\pi+\nu}(3)$ and $O_{\pi+\nu}(6)$. For more details on this formalism, we refer the reader to [6].

It is important to stress that the new degree of freedom in IBM-2 which arises from treating the protons and the neutrons separately, leads to a new symmetry called F-spin symmetry. This symmetry leads to the existence of special classes of IBM-2 eigenstates, characterized by their symmetry under the pairwise exchange of an arbitrarily chosen pair of proton and neutron bosons [31, 32]. States that are totally symmetric under this exchange are called full symmetry states (FSSs) and they correspond to the complete space of the IBM-1 model with the same total boson number, where no distinction is made between proton bosons and neutron bosons. States that contain at least one antisymmetric pair of proton and neutron bosons are called mixed-symmetry states (MSSs).

The proton-neutron boson symmetry of the IBM-2 wave functions can be quantified by the F-spin quantum number. The concept of F-spin is formally equivalent to the isospin, resulting in an assignment of an F-spin of $F = 1/2$ with projections $F_z = +1/2$ for proton and $F_z = -1/2$ for neutron bosons. For a given nucleus with fixed numbers of proton and neutron bosons, N_π and N_ν, respectively, the z-component of the F-spin is a good quantum number. Its value is $F_z = N_\pi(+1/2) + N_\nu(-1/2) = 1/2(N_\pi - N_\nu)$. The maximal F-spin is given by $F_{max} = 1/2(N_\pi + N_\nu)$. The F-spin quantifies the symmetry of a wave function under pairwise exchange of proton and neutron boson labels. Basis states that are characterized by a maximum F-spin quantum number $F = F_{max}$ can be transformed by the successive action of the F-spin raising operator F_+ into a state that consists of proton bosons only. Such a state stays obviously unchanged under a pairwise exchange of proton and neutron labels because it does not contain any neutron bosons [15]. Therefore, IBM-2 states with maximum F-spin quantum number are called Full Symmetry States (FSSs) and have $F(FSS) = F_{max}$. The

pure proton IBM-2 wave function is identical to the IBM-1 wave function for N proton bosons. All other basis states with good F-spin quantum numbers $F < F_{max}$ are outside the framework of IBM-1. These states are called proton-neutron mixed symmetry states (MSSs). The name expresses the fact that these states contain at least one antisymmetric pair of proton and neutron bosons. In fact, the F-spin quantum number counts the number of bosons that are symmetric with respect to pairwise exchange of proton and neutron labels [15]. Up to now only MSSs with quantum numbers $F = F_{max} - 1$ have ever been observed. Examples of such states are the 1^+ scissors mode [33] or 2^+ mixed-symmetry states in vibrational nuclei [15]. Excitations of lower F-spin have not yet been identified.

Since the present study is focused on the properties of the lowest MSS $2^+_{1,ms}$ in the case of U(6) symmetry, $i.e.$ of vibrational nuclei, it is convenient to present the IBM-2 Hamiltonian in the Q-phonon form. Taking into account that the residual nucleon-nucleon interaction in the spherical shell model is dominated by the pairing between identical nucleons, in the boson Hamiltonian we have a term of the type $\varepsilon_\pi \hat{n}_{d\pi} + \varepsilon_\nu \hat{n}_{d\nu}$. In addition, there is a quadrupole-quadrupole interaction between non-identical nucleons which produces a term of the type $\kappa \hat{Q}^\chi_\pi \cdot \hat{Q}^\chi_\nu$, where $Q^\chi = [d^\dagger \times \tilde{s} + s^\dagger \times \tilde{d}]^{(2)} + \chi [d^\dagger \times \tilde{d}]^{(2)}$. Finally, there is a symmetry energy which favors states in which protons and neutrons move in phase. Taking into account all properties mentioned above, the IBM-2 Hamiltonian can be represented as [6]:

$$H = E_0 + \varepsilon_\pi \hat{n}_{d\pi} + \varepsilon_\nu \hat{n}_{d\nu} + \kappa \hat{Q}^\chi_\pi \cdot \hat{Q}^\chi_\nu + \lambda' \hat{M}_{\pi\nu} \tag{2.16}$$

where

$$\hat{M}_{\pi\nu} = [s^\dagger_\nu \times d^\dagger_\pi - s^\dagger_\pi \times d^\dagger_\nu]^{(2)} \cdot [\tilde{s}_\nu \times \tilde{d}_\nu - \tilde{s}_\pi \times \tilde{d}_\nu]^{(2)} - 2 \sum_{k=1,3} [d^\dagger_\nu \times d^\dagger_\pi]^{(k)} \cdot [\tilde{d}_\nu \times \tilde{d}_\pi]^{(k)} \tag{2.17}$$

is called Majorana operator which accounts for the symmetry energy. This Hamiltonian was suggested by Talmi [32].

A simple case of vibrational nucleus with only one proton and one neutron boson ($N_\pi = N_\nu = 1$) is presented in Ref. [15]. In this case the system can be described with the following Hamiltonian:

$$H = \epsilon(n_{d\pi} + n_{d\nu}) + \lambda \hat{M} \tag{2.18}$$

In this case, the Majorana operator takes the simple form $\hat{M} = [F_{max}(F_{max}+1) - \hat{F}^2]/2$. Its structure is such that it acts on MSSs only. The resulting spectrum is shown in Fig. 2.4.

The Hamiltonian has U(5) symmetry and produces a vibrational spectrum with a symmetric $J^\pi = 2^+$ one-quadrupole phonon state and a symmetric two-phonon triplet with $J^\pi = 4^+, 2^+, 0^+$ states. The boson wave functions for this example are displayed in Fig. 2.4 as well. Besides the 2^+_1 one-quadrupole phonon FSS, there is an antisymmetric (with respect to proton-neutron labels) linear combination of the two configurations with $n_d = 1$, forming the mixed-symmetry one-quadrupole phonon $2^+_{1,ms}$ state with F-spin quantum number $F = F_{max} - 1$. Antisymmetric angular momentum coupling of two (non-identical) d-bosons leads
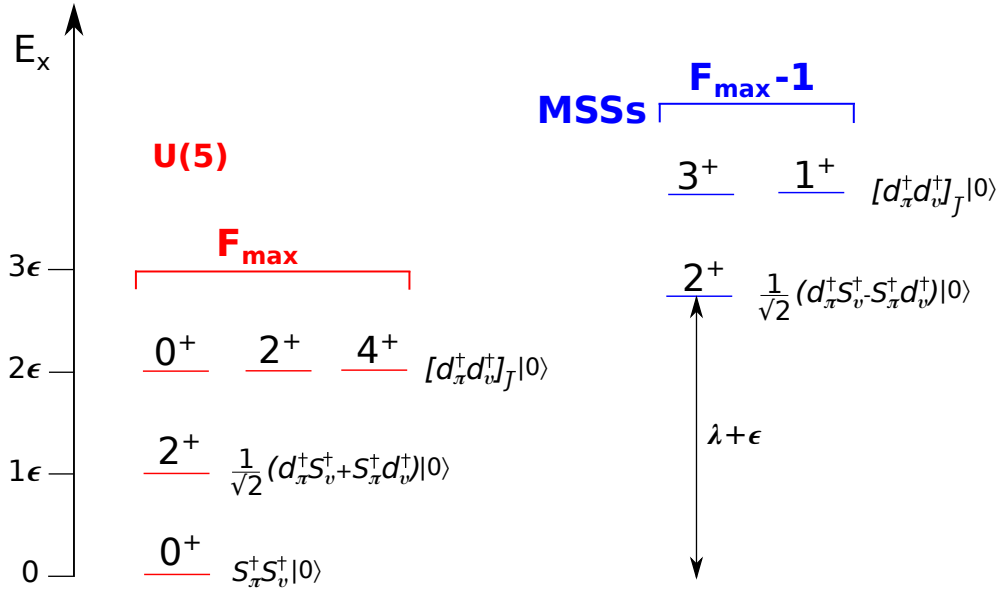
Figure 2.4: Spectrum of a schematic IBM-2 Hamiltonian with U(5) symmetry with boson numbers $N_\pi = N_\nu = 1$ from Ref. [15].

to mixed-symmetry two-phonon states with odd spin quantum numbers, 3^+ and 1^+ [25].

The experimental signature for the mixed-symmetric states is a strong $M1$ decay. This is expected due to the F-vector ($\Delta F = 1$) nature of the $M1$ transition operator, which is given by [15]

$$T(M1) = \sqrt{\frac{3}{4\pi}}[\mathrm{g}_\pi L_\pi + \mathrm{g}_\nu L_\nu]\mu_N \tag{2.19}$$

$$= \sqrt{\frac{3}{4\pi}}\left[\frac{N_\pi \mathrm{g}_\pi + N_\nu \mathrm{g}_\nu}{N}L_{tot} + (\mathrm{g}_\pi - \mathrm{g}_\nu)\frac{N_\pi N_\nu}{N}\left(\frac{L_\pi}{N_\pi} - \frac{L_\nu}{N_\nu}\right)\right]\mu_N \tag{2.20}$$

Since the operator $L_{tot} = L_\pi + L_\nu$ is diagonal in IBM-2 by construction, it cannot induce transitions between different states. g_ρ, $\rho \in \{\pi, \nu\}$, are the effective boson g-factors and $N = N_\pi + N_\nu$ is the total number of bosons. In Ref. [34] is shown that the proton-neutron contribution to the matrix elements of any one-body operator between FSSs is given by:

$$\langle F_{max}, \alpha || b_{\rho,\beta}^\dagger b_{\rho,\beta'} || F_{max}, \alpha' \rangle = N_\rho C_{\alpha\alpha'\beta\beta'} \tag{2.21}$$

where $\alpha, \alpha', \beta, \beta'$ are additional quantum numbers and N_ρ is the number of bosons of given type. $C_{\alpha\alpha'\beta\beta'}$ depends on the initial and final states only, hence, it is the same for L_π and L_ν. Thus, in the limit of F-spin symmetry no $M1$ transitions are allowed between FSSs. The situation is completely different in the case of transitions between MS and FS counterparts which are F-spin allowed. This can be easily seen from the structure of the wave functions of the one-phonon states in Fig. 2.4; the $M1$ matrix element between them is approximately equal to the difference $\mathrm{g}_\pi - \mathrm{g}_\nu$ which is of the order of $1\mu_N^2$. Experimentally the strongest $M1$ transition between one-phonon MSS and FSS is observed in ^{94}Mo and its

size is $0.56\mu_N^2$ [15]. In all other cases the $M1$ transition strength varies between 0.1 and $0.3\mu_N^2$ [15]. This comprises the main experimental signature for the one-phonon $2_{1,ms}^+$ states - since no other $M1$ transitions are allowed except for the one connecting a mixed-symmetry state to a fully-symmetric state, it provides a unique signature for experimental identification of these states [25].

The F-scalar ($\Delta F = 0$) $E2$ transition operator is given by

$$T(E2) = e_\pi Q_\pi^{\chi_\pi} + e_\nu Q_\nu^{\chi_\nu}, \qquad (2.22)$$

where e_π and e_ν are effective quadrupole boson charges, couples FSSs and FSSs or MSSs and MSSs, but is forbidden for transitions between MSSs and FSSs. Practically, the transition is never completely inhibited, but in most cases it is strongly suppressed. On the other hand, the $2_{1,ms}^+$ state is a one-phonon excitation which should have sizeable collective $E2$ matrix elements for a transition to the ground state for both protons and neutrons, but with opposite signs, which might lead to partial cancellation in the total $\langle 0^+ || E2 || 2_{1,ms}^+ \rangle$ matrix element. Thus, a weakly collective $E2$ transition strength of a few W.u. for the $2_{1,ms}^+ \to 0_1^+$ transition can be expected which constitutes another important experimental signature for MSSs [15].

From the above mentioned fingerprints it is obvious that the MSSs can be identified experimentally by their unique decay to the low-lying FSSs. This however, comprises a major experimental challenge because it requires full spectroscopic information - the spin and parity quantum numbers of these highly non-yrast states, their lifetimes, the branching ratios and multipole mixing ratios of their γ-decays [25].

Chapter 3

Search for one-phonon $2^+_{1,ms}$ state in ^{212}Po

The lifetimes of mixed-symmetry states are usually in the sub-picosecond range [15]. Therefore, the Doppler-shift attenuation method (DSAM) [35] is the method of choice for lifetime extraction. In the most commonly used version of this technique, a level is populated in a nuclear reaction and decays by emission of γ rays. The projectile partly transfers its linear momentum to the target nucleus, which is subsequently slowing down due to atomic interactions in the target material. To ensure that all recoil nuclei are completely stopped, a second layer, denoted as stopper, is added behind the target material. The stopping time is usually in the range of 1 ps and thus sets the scale for lifetimes that can be measured with this technique. The γ rays which are emitted from nuclei recoiling in matter have energies which are shifted by an amount depending on the initial velocity of the nuclei. If an excited nucleus decays while recoiling with velocity $v(t)$, then the energy of the γ rays can be expressed as

$$E_\gamma(\theta, t) = E_\gamma^0 \frac{\sqrt{1 - \beta^2(t)}}{1 - \beta(t) \cos \theta} \tag{3.1}$$

where $\beta(t) = v(t)/c$ is the ratio of the ion velocity to the speed of light, E_γ^0 is the γ-ray energy emitted by the nucleus at rest and θ is the angle of observation relative to the recoil direction. To first order in $\beta(t)$, the equation (3.1) reduces to the familiar expression

$$E_\gamma(\theta, t) = E_\gamma^0(1 + \beta(t) \cos \theta) \tag{3.2}$$

which is valid for $\beta(t) \ll 1$. In general, there will be a continuous distribution of $E_\gamma(t)$ between E_γ^0 and $E_\gamma^0(1 + \beta(0) \cos \theta)$ corresponding to decays occuring for ion velocities between 0 and $v(0)$. A schematic diagram of the Doppler shift attenuation method is presented in Fig. 3.1. The average Doppler shift depends on the lifetime of the level and on the slowing-down time of the nucleus in the stopping material. Thus, the lifetime of the level of interest can be determined from the attenuated Doppler shift if the slowing-down process is known [36].
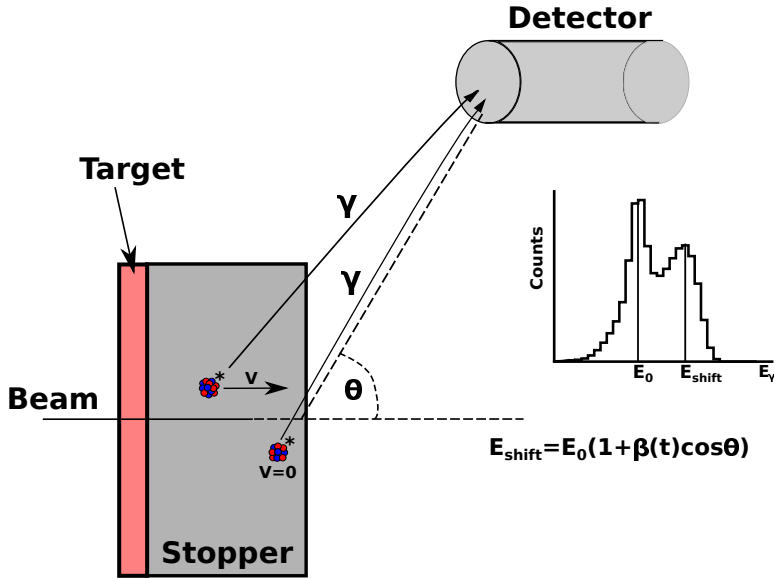
Figure 3.1: Schematic diagram of the Doppler shift attenuation method for measuring nuclear lifetimes. When the nucleus (with velocity v, $\beta = v/c$) emits γ-ray in flight, the energy of the γ-ray will be detected as $E_\gamma = E_0(1 + \beta \cos\theta)$. When the nucleus decays at rest (with velocity $v = 0$), $E_\gamma = E_0$.

3.1 Experimental set-up

As mentioned in section 1.2. the $2^+_{2,3}$ states in ^{212}Po are good candidates for the one-phonon MSS. The only missing piece of experimental information to verify this hypothesis is the large absolute $M1$ transition strengths corresponding to short lifetimes of these levels. In order to measure the lifetime of the 2^+_2 and 2^+_3 states in ^{212}Po by means of DSAM an experiment was performed at the FN Tandem facility of the University of Cologne, Germany. Excited states of ^{212}Po were populated using the transfer reaction ^{208}Pb(^{12}C,^{8}Be)^{212}Po at a beam energy of 62 MeV. The beam energy was chosen to be about 2 MeV below the Coulomb barrier. The target was a self-supporting 10 mg/cm^2 thick Pb foil enriched to 99.14% with the isotope ^{208}Pb. The reaction took place in the reaction chamber of the Cologne plunger device [38]. An array of solar cells was mounted at backward angles with respect to the beam direction, in order to detect the recoiling light reaction fragments. The solar cell array consisted of six 10 mm $\times$ 10 mm cells placed at a distance of about 15 mm between their centres and the target. The array covered an annular space between 116.8° and 167.2°. The γ rays from the decay of the excited states in ^{212}Po were registered by 12 HPGe detectors mounted outside the plunger chamber in three rings at an average distance of 12 cm from the target. Five detectors were positioned at 142.3° with respect to the beam direction, another six formed a ring at 35° and a single detector was placed at 0°. Data were taken in coincidence mode of at least one solar cell and one HPGe detector (particle-γ) or of at least two HPGe detectors ($\gamma - \gamma$).
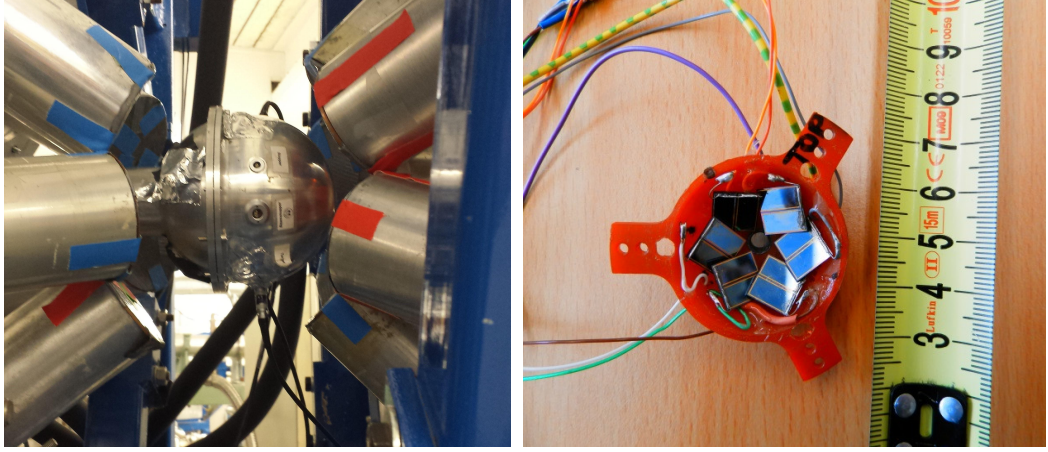
26

Figure 3.2: Experimental set-up: (left) 6 HPGe detectors at 35° and 5 HPGe detectors at 142°; (right) The solar cells array for detection of the light reaction fragments.

3.2 Data analysis

The particle-γ coincidence data were sorted in three matrices depending on the position of the HPGe detectors. A projection of the particle-γ matrix obtained with γ-ray detection at 142° is shown in Fig. 3.3(a). The γ rays in coincidence with ^{8}Be (or 2α) are shown in Fig. 3.3(b).

This spectrum is dominated by the 727-keV, the 405-keV and the 223-keV lines that are the γ-ray transitions depopulating the first three yrast states of ^{212}Po [22]. Besides some contaminants from ^{211}Po, all other γ rays in the spectrum in Fig. 3.3(b) originate from the decay of excited states of ^{212}Po [11,22,23,39,40]. A partial level scheme of the states in ^{212}Po populated in the present experiment was constructed on the basis of the γ-γ coincidence data. The level scheme is shown in Fig. 3.4. Most of these states have been identified in another α-transfer reaction, namely ^{208}Pb(^{18}O,^{14}C) [22]. In addition, we have populated two non-yrast 2^+ states at excitation energies of 1512 keV and of 1679 keV, respectively [23]. These two states decay predominantly to the 2_1^+ state via the 785-keV and the 952-keV transitions, respectively [12]. Both transitions have a well pronounced $M1$ character with multipole mixing ratios of $+0.09(3)$ and $+0.65(50)$ [23], respectively. That makes these two 2^+ states potential candidates for the one-phonon MSS in ^{212}Po.

Both the 785-keV and 952-keV lines show well-pronounced Doppler shapes which allows for lifetimes determination of the 2_2^+ and 2_3^+ states in ^{212}Po by means of the Doppler Shift Attenuation Method (DSAM).

In the DSAM, the nuclear lifetime is measured relative to the slowing down time for heavy ions in stopping materials where the changing velocity of the ions has to be accounted as well. The stopping powers for heavy ions can be separated into three velocity regions: (1) low velocity ($\beta = v/c < 0.5\%$) where nuclear stopping is the dominant mechanism for energy loss, (2) medium velocity ($\beta \sim 0.5 - 2\%$) where the competition between nuclear and electronic stopping powers is almost equal, and (3) high velocity ($\beta > 2\%$) where the electronic stopping
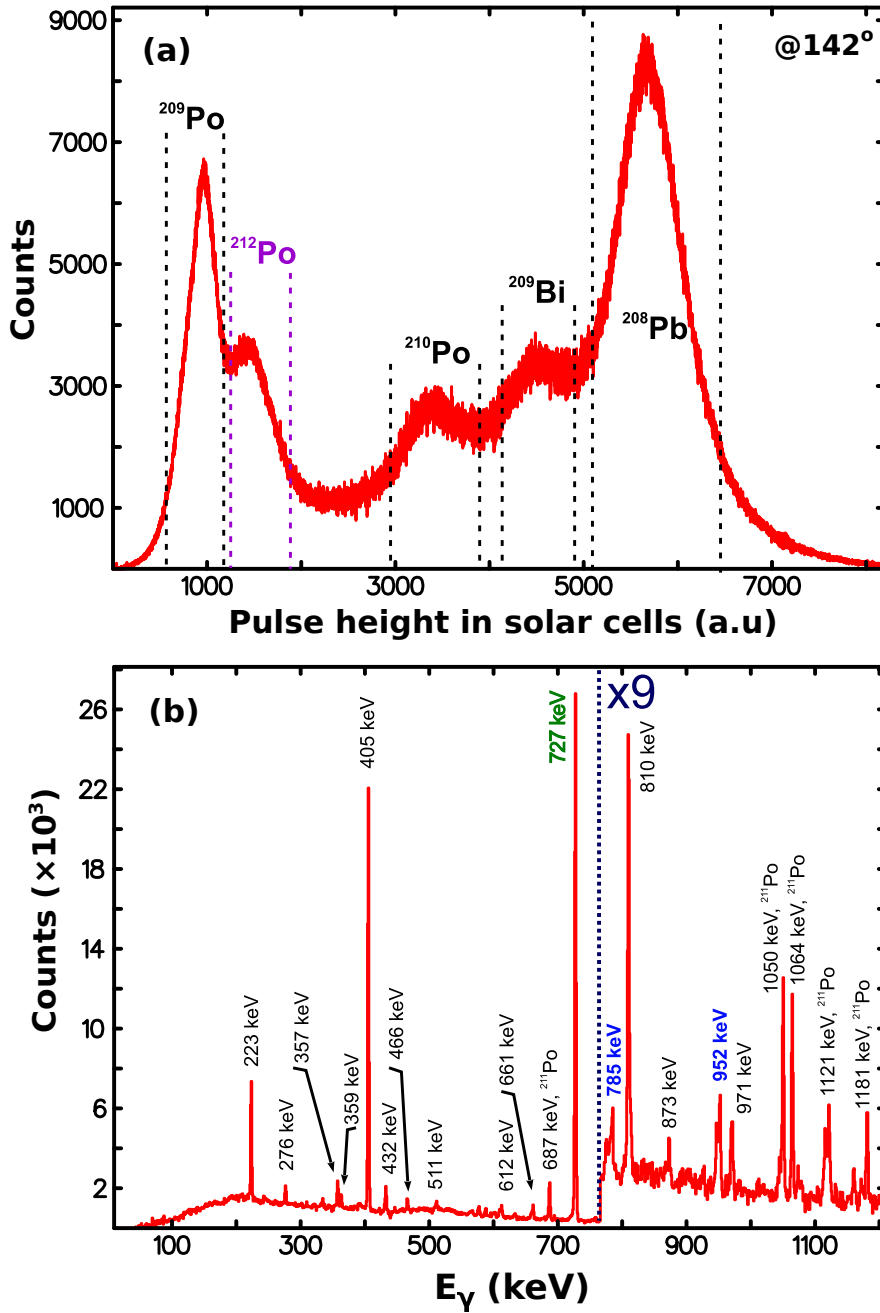
Figure 3.3: (a) The projection of the particle-γ matrix at 142°. The dashed lines represent regions in the particle spectrum found to be in coincidence with the γ rays from the indicated nuclei. (b) The γ-ray spectrum in coincidence with the group of particles indicated as "^{212}Po" in panel (a).
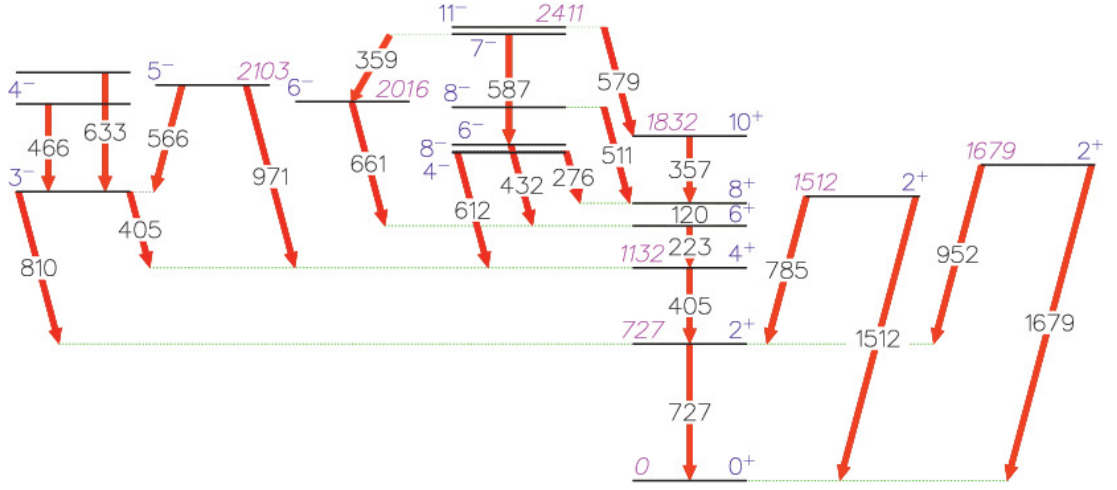
Figure 3.4: Partial level scheme of ^{212}Po obtained in the present work. The energy of the transitions are given in keV. The candidates for the one-phonon MSS are placed on the right of the yrast states

powers are dominating [35]. According to kinematics calculations performed with the program package LISE++ [41,42], the velocity of the ions of ^{212}Po is expected to be ∼ 1%, which was experimentally confirmed by measuring the maximum Doppler shift of the γ-ray. In this case, as it was mentioned above the stopping power for ^{212}Po ions results from two distinct processes: electronic and nuclear. The electronic stopping is characterized by long-range collisions, small energy transfers, and small deflections. The nuclear stopping is characterized by large energy losses and abrupt changes in direction. The widely used treatment of the slowing-down process for medium velocity ions is proposed by Lindhard, Scharff, and Schiøtt (LSS) [43]. In the LSS theory, the stopping power is defined in terms of energy ϵ and range ρ parameters. Thus

$$\frac{d\epsilon}{d\rho} = f_e \left(\frac{d\epsilon}{d\rho}\right)_e + f_n \left(\frac{d\epsilon}{d\rho}\right)_n \qquad (3.3)$$

with

$$\epsilon = E \frac{aM_2}{Z_1 Z_2 e^2 (M_1 + M_2)} \qquad (3.4)$$

and

$$\rho = RN M_2 4\pi a^2 E \frac{M_1}{(M_1 + M_2)^2} \qquad (3.5)$$

where E is the ion kinetic energy, Z_1 and M_1 are the atomic number and mass of the moving ion, Z_2 and M_2 are the atomic number and mass of the stopping material, N is the number of stopping atoms/cm^3, R is the ion range, and the screening parameter $a = 0.8853 a_0 (Z_1^{2/3} + Z_2^{2/3})^{-1/2}$. The factors f_e and f_n in equation (3.3) have been inserted as parameters to be determined from experiment. In Ref. [44–46] has been shown that the nuclear stopping power is overestimated in the LSS theory by a factor of 30%.

In order to describe the slowing down of the recoiling ^{212}Po we have performed

29

two parallel analyses of the line shapes; in the first analysis, labelled here as Analysis I, we used a Monte Carlo (MC) simulation by means of a modified [47,48] version of the program DESASTOP [49]. The electronic stopping powers used were obtained from the Northcliffe and Schilling tables [50] with corrections for the atomic structure of the medium, as discussed in Ref. [51]. An empirical reduction of $f_n = 0.7$ was applied [52] to downscale the nuclear stopping powers predicted by the LSS theory [43].

The second analysis, labelled as Analysis II, uses an integrated software named APCAD (Analysis Program for Continuous Angle DSAM) [53,54]. In APCAD, the slowing down process is simulated by the program StopSim which is based on GEANT4 [55]. Here the electronic stopping process is modelled in the same way as in Analysis I. On the other hand, APCAD adopts a simpler approach to modelling the nuclear stopping process, as compared with the completely discrete approach used in Analysis I. In Analysis II the angular straggling due to nuclear collisions is modelled discretely by means of MC simulation while the corresponding energy loss is considered to emerge as a result from a continuous process as the nuclear stopping powers were taken from SRIM2013 [56] and reduced by 30%. In Fig. 3.5 the electronic and nuclear stopping powers for ^{212}Po ions in lead material are shown, used in the program APCAD.

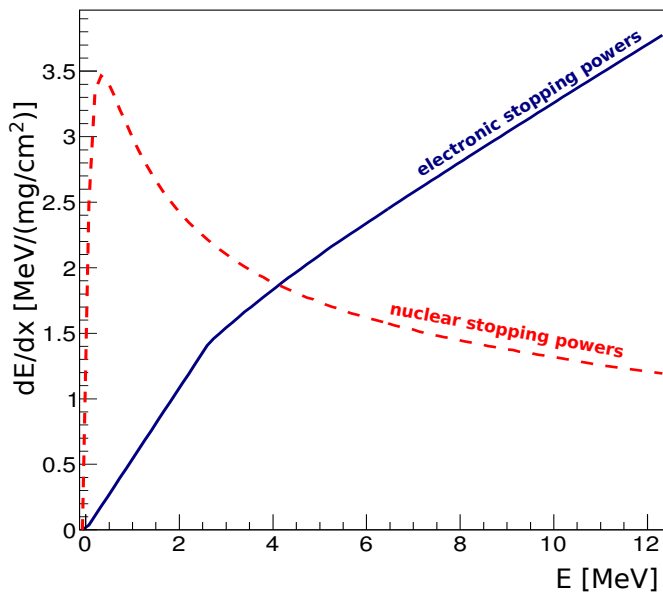Figure 3.5: The electronic (blue line) and nuclear (dashed red line) stopping powers for ^{212}Po ions slowing down in ^{208}Pb as a function of the ions energy.

The output of the simulation is a set of ion velocity histories. They contain the velocity vectors of individual ions in an ensemble, sampled in time steps. The velocity histories start at the time of excitation of the ions ($t = 0$) and end at the time when the ions come to rest inside the target or leave it. These velocity histories are the starting point for calculating Doppler-broadened γ-ray line-shapes. The temporal evolution of the velocity distribution for an ensemble of ^{212}Po ions provided by StopSim is shown in Fig. 3.6.

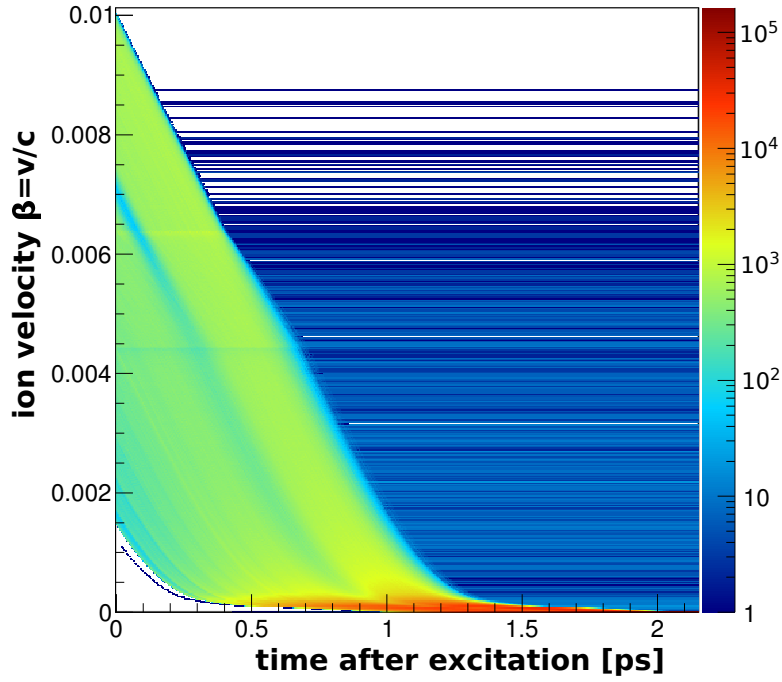The particle-γ coincidence requirement leads to restrictions on the reaction

Figure 3.6: Temporal evolution of the velocity distribution for ions of ^{212}Po which are excited at $t = 0$ and slowed-down in a target of 10 mg/cm^2 lead foil.

kinematics imposed by the solar cell array (see Fig. 3.7). In terms of the simulation this means that only events for which the projectile-like product of an excitation reaction leaves the target are recorded. Therefore, ion velocity histories can be selected according to the kinematics of reaction products ejected from the target and hit the defined particle detector [54].
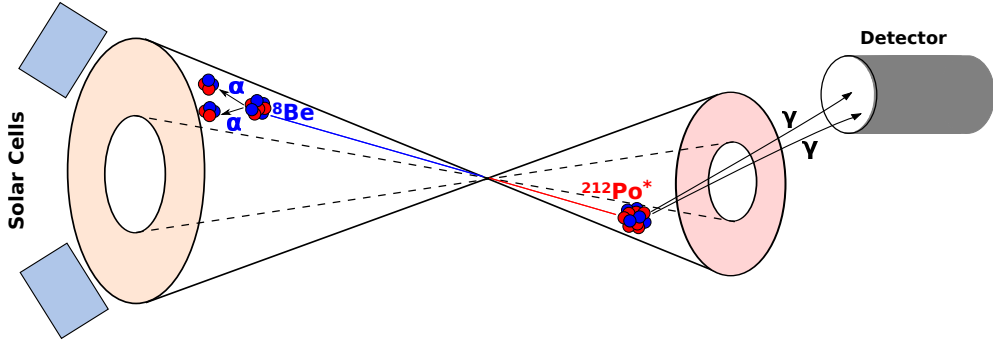

Figure 3.7: Schematic representation of the cases when the detector system fires coincidences between the light reaction fragments (detected by the solar cells) and γ rays coming from the excited states of the nucleus ^{212}Po (registered by HPGe detectors). Both cones are imaginary and represent the solid angles at which the reaction fragments should move in order to be detected taking into account the annular space covered by the solar cell array.

All available information on detector and set-up geometry, excitation and slowing-down process is contained into pre-calculated distribution functions that describe theoretical Doppler-shift distributions as a function of the time of γ-ray

emission. These distributions are stored in the form of the so-called stopping matrices. The stopping matrices contain the information of what distribution of Doppler-shifts would be registered by the γ-ray detectors at certain angles, if γ-ray emission would occur at a certain time after the excitation reaction. These distributions are discretized in both Doppler-shift and time. The discretization in time is given by the time steps of the velocity histories. The stopping matrices are calculated for each angular detector ring (see Fig. 3.8). Sums of these stopping matrices over time, weighted by decay functions, yield the distributions of Doppler-shifts occurring for individual γ-ray transitions. From both these distributions and given unshifted γ-ray energies, spectra of γ-rays hitting the γ-ray detectors are obtained. Taking into account the detector response functions and the feeding histories of the levels of interest the final calculated spectra with the Doppler-broadened line-shapes could be compared to experimental data [54].

In our analysis the feeding histories of the levels of interest were determined from the $\gamma - \gamma$ coincidence data. Slow feeding was introduced and fitted in the analyses only if the analysed transitions were observed in coincidence with transitions from higher-lying states. Otherwise, only very fast feeding which can be associated with direct population of the levels of interest, was considered.

Before extracting the lifetimes of the states of interest we verified our analyses with a previously known lifetime. For example, the lifetime of the 6^- state at 2016 keV is known to be 0.49(16) ps [22]. Under the above assumptions both analyses produced similar results. The lifetime of this level derived in our analysis from the line-shape of the 661.3-keV transition, with a feeding history similar to the one used in Ref. [22] (58% fast feeding and 42% slow feeding), is 0.50(4) ps in Analysis I and 0.46(4) ps in Analysis II, respectively. This consistency allowed us to conclude that we can determine the lifetimes of the $2^+_{2,3}$ states correctly.

The lifetimes of the 2^+_2 state at 1512 keV and the 2^+_3 state at 1679 keV were extracted from the line shapes of the 785-keV and the 952-keV transitions, respectively. Both of these transitions are in coincidence with the 727-keV ($2^+_1 \rightarrow 0^+_1$) transition, only (see Fig. 3.4). Therefore only fast feeding ($\tau_{feeding} \leq 10$ fs) was introduced in the fits of their line shapes. In Fig. 3.9, examples of these fits obtained with the program APCAD are presented. The final lifetimes together with the available spectroscopic information and the resulting transition strengths are summarized in Table 3.1. The quoted uncertainties of the results for the lifetimes from Analysis I and II include statistical uncertainties from the line-shape fits and 10% uncertainty in the nuclear and electronic stopping powers. The adopted values are taken as average between the results from both analyses.

3.3 Interpretation of the results

As seen from Table 3.1, the 2^+_2 state in ^{212}Po at 1512-keV excitation energy decays with a sizeable $M1$ transition to the 2^+_1 state. This allows us to conclude that the 2^+_2 state in ^{212}Po has isovector nature and as such it can be considered, at least, as a fragment of the one-phonon MSS. This represents the first identification of a low-lying isovector state in a nucleus from the mass region around the double-magic nucleus ^{208}Pb. On the other hand, all observed $B(E2)$ strengths in the
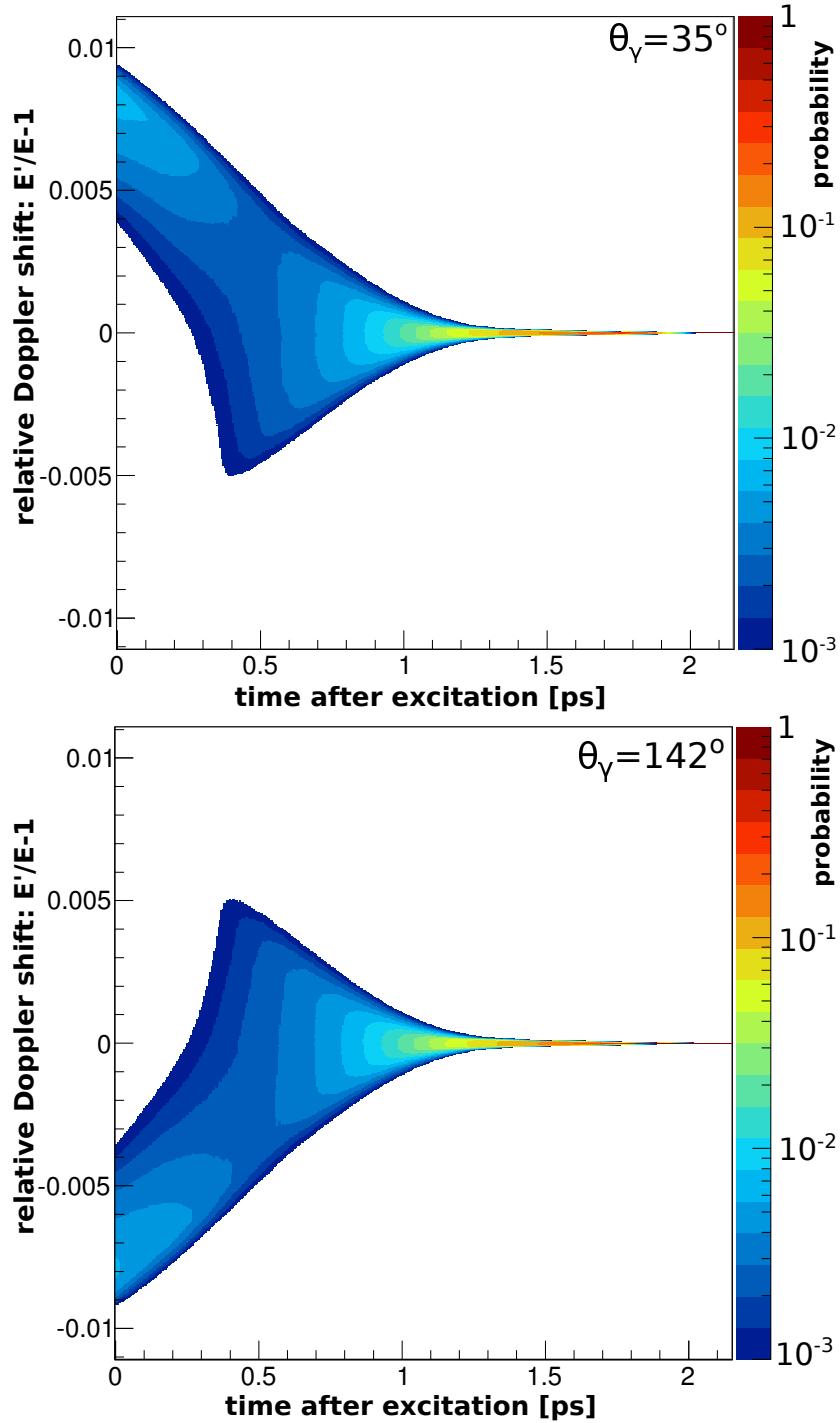
Figure 3.8: Stopping matrices for the angular bins centered at 35° (upper panel) and 142° (bottom panel). It shows the intensity distribution of relative Doppler-shifts that would be registered in this angular bins as a function of time of the γ-ray emissions after the excitation reaction. E' is the Doppler-shifted γ-ray energy and E denotes the transition energy that is observed if the emission occurs at rest.
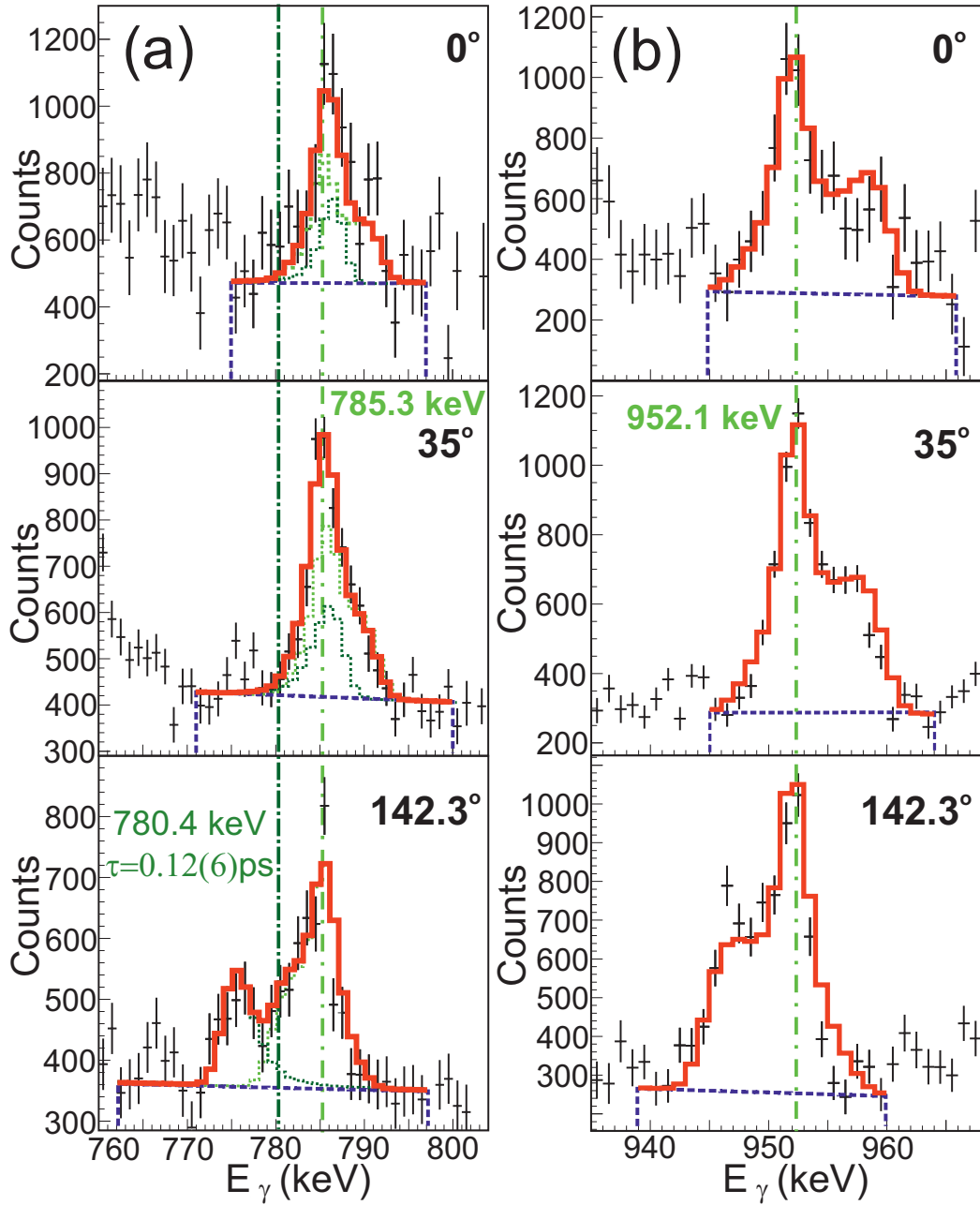
Figure 3.9: An example of line-shape fits of the 785.3-keV ($2_2^+ \rightarrow 2_1^+$)(a) and the 952.1-keV ($2_3^+ \rightarrow 2_1^+$) (b) transitions obtained with the program APCAD. The dashed (blue) lines show the background and the fit regions. The solid (red) line represents the total fit. The 785-keV line is fitted simultaneously with the 780.4-keV line which originates from the decay of the $7^{(+)}$ state in ^{212}Po at the excitation energy of 3155 keV ($\tau = 0.12(6)$ps) [22]. The dotted lines (green and grass green) represent the individual contributions of 785-keV and 780-keV lines to the total fit. The vertical dash-dotted lines show the position of the unshifted peaks.

Table 3.1: Properties of the 2_2^+ and the 2_3^+ states in ^{212}Po and γ-ray transitions originating from their decays. Given are the excitation energies (E_{level}), the spin and parity quantum numbers of the initial levels (J_i^π) and of the final levels (J_f^π), the relative intensities (I_γ), and the multipole mixing ratios (δ), the lifetimes of the states, and the absolute transition strengths. For calculating the absolute transition strengths the total electron conversion coefficient α from Ref. [12] were used.

E_{level} (keV)	J_i^π	J_f^π	$I_\gamma{}^a$ %	δ^b	τ (ps) An. I	τ (ps) An. II	τ (ps) Adopted	Transition strength ^{c} $J_i^\pi \to J_f^\pi$
1512	2_2^+	0_1^+	26(3)		0.73(7)	0.69(6)	0.71(9)	$B(E2) = 29(4)$
		2_1^+	100(1)	0.09(3)				$B(M1) = 0.126(16)$
								$B(E2) = 24(16)$
1679	2_3^+	0_1^+	35(8)		0.82(4)	0.74(7)	0.78(8)	$B(E2) = 20(5)$
		2_1^+	100(19)	0.65(50)				$B(M1) = 0.042(20)$
								$B(E2) = 290(273)$

^{a}From Ref. [12].
^{b}From Ref. [11]
$^c B(E2)$ values are given in e^{2}fm^4 (1 W.u.= 75.09 e^{2}fm^4), and the $B(M1)$ values are given in μ_N^2. In the calculations for the transitions strengths vanishing α-decay branches were assumed.

decays of the 2_2^+ and the 2_3^+ states are low (cf. Table 3.1). These observations indicate a lack of quadrupole collectivity in these low-energy states and question the applicability of the phonon picture in ^{212}Po. In order to check this hypothesis shell model calculations have been done. They are based on the simplest possible description of the low-lying states of ^{212}Po which can be pursued in the framework of an empirical single-j shell model approximation.

3.3.1 Single-j shell model calculations with effective charges fixed to the $B(E2; 8_1^+ \to 6_1^+)$ values in ^{210}Po and ^{210}Pb

The nucleus ^{212}Po has two neutrons and two protons outside the ^{208}Pb core. In this approach, the two neutrons are in the $2g_{9/2}$ shell and the protons are in the $1h_{9/2}$ shell. The interactions between the valence particles as well as the effective electromagnetic operators are derived from the experimental data for the neighbouring nuclei as follows. In the single-j shell approximation, ^{210}Pb corresponds to two neutrons in the $2g_{9/2}$ orbital while ^{210}Po corresponds to two protons in the $1h_{9/2}$ orbital with respect to the ^{208}Pb core. Both these nuclei display seniority spectra [57] that are consistent with the single-shell hypothesis. The energy spectrum of ^{210}Bi determines the interaction between a neutron in the $2g_{9/2}$ orbital and a proton in the $1h_{9/2}$ orbital, and the entire multiplet from 0^- to 9^- is known [57]. In the single-j shell approximation, the basis states of ^{212}Po can be written as $|(2g_{9/2})^2 J_\nu, (h_{9/2})^2 J_\pi; J\rangle \equiv |J_\nu J_\pi J\rangle$. The proton-proton and neutron-neutron interactions are diagonal in this basis which is mixed by the proton-neutron interaction,

$$\langle J_\nu J_\pi J | \hat{H} | J'_\nu J'_\pi J \rangle = (V_{\nu\nu}^{J_\nu} + V_{\pi\pi}^{J_\pi})\delta_{J_\nu J'_\nu}\delta_{J_\pi J'_\pi} +$$

$$+ 4\sqrt{(2J_\nu + 1)(2J_\pi + 1)(2J'_\nu + 1)(2J'_\pi + 1)} \times$$

$$\times \sum_R (2R+1) \begin{bmatrix} j_\nu & & j_\pi & & J_\pi & & J_\nu & \\ & R & & j_\pi & & J & & j_\nu \\ j_\nu & & j_\pi & & J'_\pi & & J'_\nu & \end{bmatrix} V_{\pi\nu}^R,$$

where $V_{\nu\nu}^{J_\nu}$, $V_{\pi\pi}^{J_\pi}$, and $V_{\pi\nu}^R$ are the neutron-neutron, proton-proton and proton-neutron interaction matrix elements, respectively; the symbol in square brackets is a 12j coefficient of the second kind [58]. In the single-j shell approximation the $M1$ operator is entirely determined from the magnetic moments of the ground states of ^{209}Pb and ^{209}Bi, $\mu(9/2_1^+) = -1.4735(16)\mu_N$ and $\mu(9/2_1^-) = +4.1103(5)\mu_N$ [59]. This yields a neutron g factor of g$_\nu$ = -0.33 and a proton g factor of g$_\pi$ = $+0.91$. In ^{210}Pb and ^{210}Po there are several known $B(E2)$ values for transitions between the lowest-lying yrast states. Amongst them, the lowest $B(E2)$ values are observed for the $8_1^+ \rightarrow 6_1^+$ transitions, $53(23)$e^{2}fm^4 in ^{210}Pb and $84(3)$e^{2}fm^4 in ^{210}Po. Consequently, it can be assumed that the 8_1^+ and 6_1^+ states of these nuclei have pure two-nucleon configurations. Therefore, the effective proton and neutron charges in the $E2$ transition operator were determined from the measured $B(E2; 8_1^+ \rightarrow 6_1^+)$ values for ^{210}Pb and ^{210}Po. This approach yields the effective charges $e_\nu = 1.04$ and $e_\pi = 1.52$.

In Fig. 3.10 the calculated level energies are compared with the experimental ones. It can be seen that the yrast states of ^{212}Po form a seniority-like excitation pattern. The energies for most of the states, except for 10_1^+ and 2_3^+, are well reproduced. Apparently, the 10_1^+ and 2_3^+ states have more complicated structures outside the considered model space. For the rest of the states, the calculated spectrum closely follows the experimentally-observed energy pattern with some energy compression. The latter leads to deviations between the observed and the calculated level energies in the range between 37 keV (for the 2_1^+) to 150 keV (for the 2_2^+). The 2_2^+ state is correctly reproduced to appear slightly higher than the 8_1^+ state. We stress that this description is not a fit to the data on ^{212}Po but rather, an extrapolation of the data on neighbouring nuclides to ^{212}Po based on the hypothesis of a structure dominated by the $1h_{9/2}$ and $2g_{9/2}$ orbitals.

The comparison between the experimental transition strengths and the calculated ones for decays of the low-lying states in ^{212}Po is shown in Table 3.2. The agreement between the experimental and the calculated transitions strengths for the non-yrast states is good, qualitatively, even for the 2_3^+ state. More importantly, the model predicts that the 2_2^+ state decays with a very strong $M1$ transition to the 2_1^+ state - in qualitative agreement with the observed sizeable value of $0.126(16)\mu_N^2$. Thus, the model accounts qualitatively well for the main isovector features of the low-lying states in ^{212}Po which allows to trace the origin of the $M1$ strength to the structure of the 2_1^+ and 2_2^+ states. The wave functions of these states can be presented as follow:
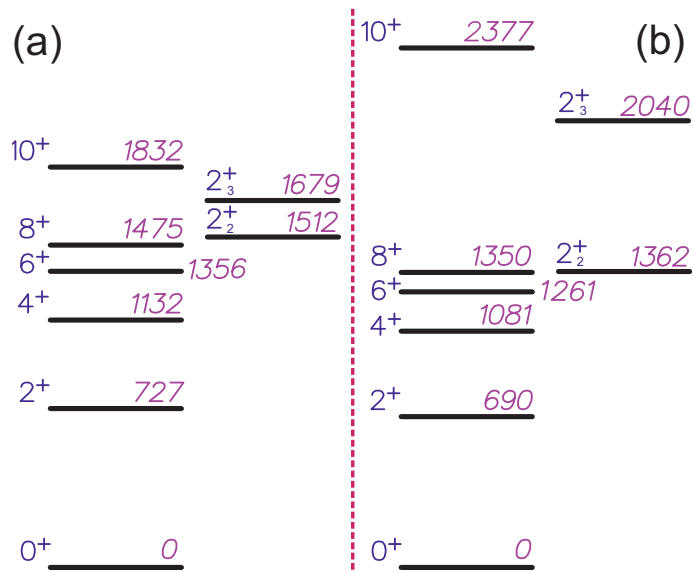
Figure 3.10: Comparison of experimental low-lying excited states in ^{212}Po (a) with the calculated ones (b). The energies of the levels are given in keV.

Table 3.2: Comparison between the experimental and the calculated transition strengths for decays of the low-lying states in ^{212}Po.

Transition $J_i \to J_f$	$B(M1; J_i \to J_f)(\mu_N^2)$ Experiment	Theory	$B(E2; J_i \to J_f)(\text{e}^2\text{fm}^4)$ Experiment	Theory
$2_1^+ \to 0_1^+$	–	–	–	463
$4_1^+ \to 2_1^+$	–	–	–	533
$6_1^+ \to 4_1^+$	–	–	293 $(83)^a$	300
$8_1^+ \to 6_1^+$	–	–	173 $(68)^a$	103
$10_1^+ \to 8_1^+$	–	–	165 $(45)^a$	75
$2_2^+ \to 0_1^+$	–	–	29 $(4)^b$	59
$2_2^+ \to 2_1^+$	0.126$(16)^b$	0.46	24 $(16)^b$	17
$2_3^+ \to 0_1^+$	–	–	20 $(5)^b$	7
$2_3^+ \to 2_1^+$	0.042$(20)^b$	0.0003	290 $(273)^b$	186

^{a}From data given in Ref. [12].
^{b}From the present work (cf. Tab. 3.1).

$$\begin{aligned} |2_1^+\rangle &= 0.448|J_\nu = 0, J_\pi = 2, J = 2\rangle + 0.819|J_\nu = 2, J_\pi = 0, J = 2\rangle + \cdots \\ |2_2^+\rangle &= 0.813|J_\nu = 0, J_\pi = 2, J = 2\rangle - 0.517|J_\nu = 2, J_\pi = 0, J = 2\rangle + \cdots \end{aligned}$$

The two components in the wave functions, which can be thought of as proton and neutron S and D pairs, exhaust about 87% and 93% of the total wave functions of the 2_1^+ and the 2_2^+ states, respectively. These two states are almost orthogonal as the main difference between these wave functions is the opposite sign of the dominant proton and neutron components. This reveals the isovector nature of the wave function of the 2_2^+ state which leads to the enhanced $B(M1; 2_2^+ \to 2_1^+)$ value. Apparently, even extremely simple shell models, like the one used here, tend to generate low-lying isovector state in agreement with the experimental observation. At the same time both the experimental results and the theoretical calculation indicate an anomalously low quadrupole collectivity in ^{212}Po. Together these two facts suggest that the isovector nature is a property of the valence shell configuration and does not need collectivity to appear at low excitation energy.

Chapter 4

Lifetime measurement of the first 2^+ state in ^{212}Po

In the previous chapter it has been shown that a phenomenological single-j shell model accounts very well for the properties of low-lying states, including the off-yrast 2^+ isovector state. Both experimental results and theoretical calculations hint for a low quadrupole collectivity in ^{212}Po. This raises the question whether the properties of the $2_1^+ - 4_1^+ - 6_1^+ - 8_1^+$ yrast sequence in ^{212}Po, which forms a seniority-like energy pattern (see Tab. 3.2), are entirely consistent with the seniority scheme. To address these questions experimental information on the absolute $B(E2)$ strengths for the $2_1^+ \rightarrow 0_1^+$ and the $4_1^+ \rightarrow 2_1^+$ transitions is needed. This has motivated us to perform an experiment especially designed to measure the lifetime of the 2_1^+ state of ^{212}Po.

The lifetime of the 2_1^+ state of ^{212}Po was measured by utilizing the Recoil Distance Doppler Shift (RDDS) method [35,60]. The RDDS method is a well known technique suitable for determination of lifetimes of excited nuclear states in the picosecond region. In this method, excited nuclei from a nuclear reaction in a thin target recoil into vacuum with velocity v. The nuclei travel a distance D in vacuum and are stopped in a thick stopper. The excited nuclei that survive the time of flight ($t = D/v$) in vacuum decay in the stopper material. They emit γ rays that are unshifted in energy. The γ rays from nuclei decaying in flight are Doppler shifted (see Fig. 4.1). The method uses the timing information contained in the splitting of the intensity of a depopulating γ-ray transition into components characterized by different Doppler shifts. The evolution of the intensities of the two components as a function of the target-to-stopper distance is sensitive to the lifetime τ of the depopulated level. For extracting the lifetime of the decaying state the velocity v of the recoiling nuclei needs to be known. This velocity can be either calculated by using the reaction kinematics or directly measured from the observed Doppler shift.

Although there are no difficulties in principle in the conventional analysis of RDDS data even in the case when a level is fed by many transitions from higher lying levels, it has turned out that in practice the conventional analysis can become cumbersome because it consists of fitting all observed decay curves by a set of coupled differential equations. Therefore, a transparent method for analysis of RDDS data has been proposed by A. Dewald [61], the so-called Differential
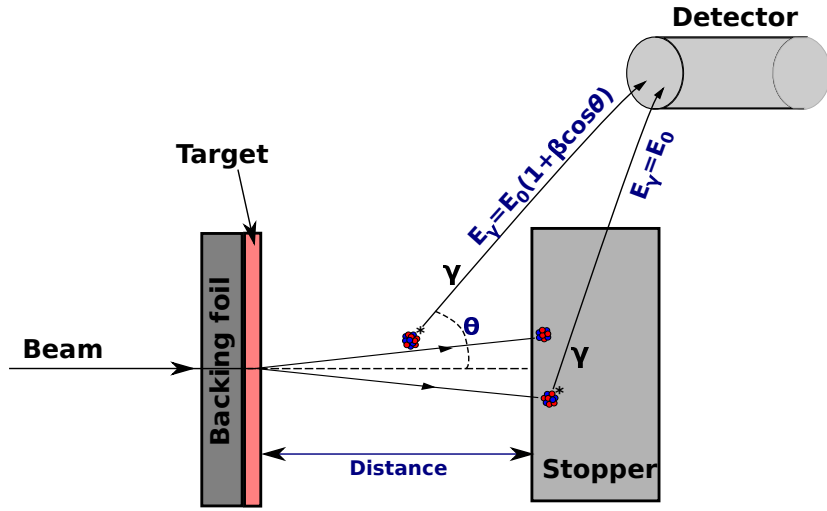
Figure 4.1: Schematic diagram of the recoil distance method of measuring nuclear lifetimes. The Doppler-shifted γ-rays can be resolved from the unshifted ones. When the nucleus (with velocity v, $\beta = v/c$) emits γ-ray in flight, the energy of the γ-ray will be detected as $E_\gamma = E_0(1 + \beta \cos\theta)$. When the nucleus decays at rest (with velocity $v = 0$), $E_\gamma = E_0$.

Decay Curve Method (DDCM). In this method the set of coupled differential equations is replaced for each individual level by a single first order differential equations of quantities, which can be directly obtained from the experimental data, if all feeders for the level of interest are known. A full description of the method can be found in Refs. [61, 62]. For completeness the model is briefly described below.
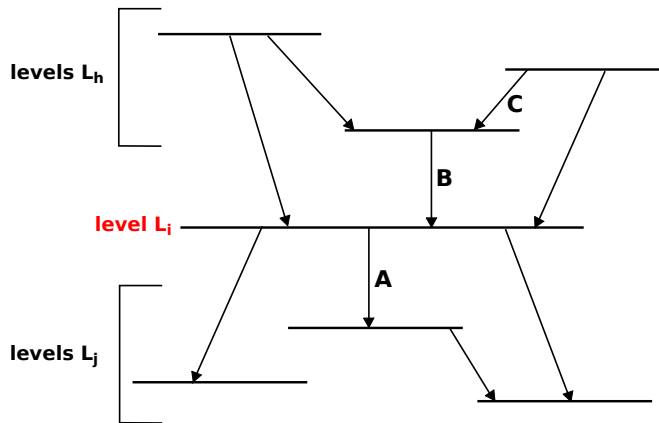
Figure 4.2: Schematic decay scheme

In Fig. 4.2 is shown an arbitrary situation for a decay and feeding pattern of a level L_i which lifetime has to be determined. The level of interest L_i is fed from higher lying levels L_h by several transitions and is depopulated by other transitions to lower lying levels L_j. The time evolution of the population $n_i(t)$ of the state L_i is given by the well known differential equation:

$$\frac{\mathrm{d}}{\mathrm{d}t}n_i(t) = -\lambda_i n_i(t) + \sum_h \lambda_h n_h(t) b_{hi} \qquad (4.1)$$

where λ_a denotes the decay constant of a level and b_{hi} are the branching ratios of the levels L_h with respect to the level L_i.

Integrating the equation 4.1 and taking into account the relation $\lambda_i = \frac{1}{\tau_i}$ one obtains the basic relation for determination of the lifetimes:

$$\tau_i(t) = \frac{-N_i(t) + \sum_h b_{hi} N_h(t)}{\frac{\mathrm{d}}{\mathrm{d}t} N_i(t)} \qquad (4.2)$$

The quantities $N_i(t)$ and $N_h(t)$ are directly proportional to the counts in the shifted and unshifted peaks observed in the RDDS data which allows the lifetime, in a singles measurement, to be directly extracted from the spectra if all feeders are known. In the cases of coincidence measurements, the feeding pattern can be simplified by gating on one feeding transition only. Then problems like the unobserved feeding which can create systematic errors in the determination of lifetimes are eliminated.

The quantities in a 2-fold-coincidence experiment are the number of events of two simultaneously observed transitions which are emitted from the same nucleus. The measured intensities of these transitions in coincidence X and Y, where transition Y occurs first, are indicated by $\{Y, X\}$. The coincidence intensities $\{Y, X\}$ can be written as:

$$\{Y_0^\infty, X_0^\infty\} = \{Y_0^t, X_0^t\} + \{Y_0^t, X_t^\infty\} + \{Y_t^\infty, X_0^t\} + \{Y_t^\infty, X_t^\infty\} \qquad (4.3)$$

Due to the time order of the transitions the intensity $\{Y_t^\infty, X_0^t\}$ is equal to zero since a nucleus at rest after the transition Y_t^∞ can not decay in flight afterwards.

In order the formulas for determining of the lifetimes from the observed coincidence intensities to be derived the notation in Fig. 4.2 is used. The decay which is observed to measure the lifetime of the level i is transition A. The first transition we will discuss is in a coincidence with a higher lying transition C that feeds the level i via one intermediate transition.

$$\tau_i(t) = \frac{\{C_0^t, A_t^\infty\} - \{C_0^t, B_t^\infty\} \frac{\{C_0^t, A_0^\infty\}}{\{C_0^t, B_0^\infty\}}}{\frac{\mathrm{d}}{\mathrm{d}t}\{C_0^t, B_0^t\}} \qquad (4.4)$$

In RDDS experiments the time scale is represented by the flight time t of the excited nuclei from the target to the stopper. The quantity X_0^t in the RDDS case is given by the intensity of the shifted component of a transition for which the intuitive notation X_{sh} will be used. Analogously X_t^∞ corresponds to the unshifted components X_{un}, and for X_0^∞ the notation X_{us} is used. For clarity, the equation 4.4 can be rewritten in terms of shifted and unshifted components with the following formula:

$$\tau_i(t) = \frac{\{C_{sh}, A_{un}\} - \{C_{sh}, B_{un}\} \frac{\{C_{sh}, A_{us}\}}{\{C_{sh}, B_{us}\}}}{\frac{\mathrm{d}}{\mathrm{d}t}\{C_{sh}, B_{sh}\}} \qquad (4.5)$$

The most important special case is that of a coincidence with a direct feeder, *i.e.* transition B in Fig. 4.2. In this case the lifetime of the state of interest L_i is determined from:

$$\tau_i(t) = \frac{\{B_{sh}, A_{un}\}}{\frac{\mathrm{d}}{\mathrm{d}t}\{B_{sh}, A_{sh}\}}. \tag{4.6}$$

The last equation can be easily rewritten in terms of the velocity of the recoiling nuclei as follows:

$$\tau_i(x) = \frac{\{B_{sh}, A_{un}\}}{v\frac{\mathrm{d}}{\mathrm{d}x}\{B_{sh}, A_{sh}\}}. \tag{4.7}$$

This lifetime formula clearly shows the simplicity of the application of the DDCM for coincidence measurement.

4.1 Experimental set-up

For measuring the lifetime of the 2_1^+ state in ^{212}Po by means of RDDS method an experiment was performed at the FN Tandem facility at the University of Cologne, Germany. The excited states of ^{212}Po were populated using the same α-transfer reaction from the previous experiment, namely ^{208}Pb(^{12}C,^{8}Be)^{212}Po. The target consisted of a 0.6 mg/cm^2 thin layer of Pb (enriched up to 99.14% with the isotope ^{208}Pb) evaporated on a 2 mg/cm^2 thick Au backing foil and was placed with the Au facing the beam. The beam energy of 64 MeV was chosen in such a way that the energy at which the reaction takes place after the Au backing to be about ~ 62 MeV. The reaction was induced in the reaction chamber of the Cologne coincidence plunger device [38]. The stopper was a self-supporting 2 mg/cm^2 thick Au foil. Data were taken at six plunger distances: 25 μm, 35 μm, 43 μm, 55 μm, 70 μm and 100 μm.

For detecting the light reaction fragments six solar cells (10 mm $\times$ 10 mm) were used. The array of solar cells was mounted in the plunger chamber at backward angles with respect to the beam axis, covering an angular range between 116.8° and 167.2°. The solar cells were placed at a distance of about 15 mm between their centres and the target. The γ rays from the decay of the excited states of ^{212}Po were registered by 11 HPGe detectors mounted outside the plunger chamber in two rings at on average distance of 12 cm from the target. Five detectors were positioned at backward angles (142.3° with respect to the beam axis) and the other six detectors were placed at forward angles (45° with respect to the beam axis). Data were taken in coincidence mode of at least one solar cell and one HPGe detector (particle-γ) or of at least two HPGe detectors (γ-γ).

4.2 Data analysis

The particle-γ coincidence data were sorted in twelve matrices depending on the positions of the HPGe detectors and the plunger distances. A projection of the particle-γ matrix obtained with γ-ray detection at 142° at plunger distance of

43 μm is shown in Fig. 4.3(a) as an example. The γ rays in coincidence with the group of particles indicated as "^{212}Po & ^{200}Tl" in Fig. 4.3(a) are shown in Fig. 4.3(b). This spectrum is dominated by transitions from excited states of ^{200}Tl which is produced by the ^{197}Au(^{12}C,$2\alpha n$) transfer reaction in the backing or in the stopper. However, the 727-, 405-, and 223-keV lines which are the γ-ray transitions depopulating the first three yrast states of ^{212}Po [11, 22] are also clearly visible. Moreover, it is also visible from Fig. 4.4 that the 727-keV transition between the 2_1^+ state in ^{212}Po and its ground state, has a well pronounced shifted component which evolves as a function of plunger distance.

The evolution of the intensities of the shifted (I_{sh}) and the unshifted (I_{un}) components of the 727-keV line with respect to the change of the plunger distances is sensitive to the lifetime of the 2_1^+ state in ^{212}Po. The RDDS data for this transition was analysed by utilizing DDCM [61,62]. As mentioned in the previous section the standard application of DDCM requires the I_{sh} and I_{un} components (for each distance) to be measured from spectra in coincidence with the Doppler-shifted components of transitions that feed directly the excited state of interest. Then the lifetime τ_i of the level of interest for the i-th target-to-stopper distance depends on I_{sh} and I_{un} in the simple way [61,62]:

$$\tau_i(x) = \frac{I_{un}(x)}{\langle v \rangle \frac{d}{dx} I_{sh}(x)} \tag{4.8}$$

as here the derivative of the Doppler shifted intensities as a function of the target-to-stopper distance, $\frac{d}{dx} I_{sh}$, is determined by a piecewise polynomial fit to the measured intensities I_{sh}. For the present experiment this would require analysing particle$-\gamma-\gamma$ data which is not possible at the acquired level of statistics. However, the particular feeding pattern of the 2_1^+ state in ^{212}Po in the used transfer reaction allows this problem to be circumvented as described below.

Figure 4.4 shows particle-gated γ-ray spectra of the $2_1^+ \rightarrow 0_1^+$ transition observed at backward (a) and forward (b) angles at three different distances. The spectra are normalized with respect to the total number of counts in the particle gate (cf. Fig. 4.3(a)) and, as a result, the total number of counts in the 727-keV transition (the sum of the shifted and the unshifted components) remains constant for all distances. At the same time, the increase of the intensity of the shifted component I_{sh} with increasing target-to-stopper distance is also apparent. However, the presented particle-gated spectra are, in fact, γ-ray singles spectra. Such spectra, in principal, contain only information for the so called effective lifetime of the 2_1^+ state of ^{212}Po which aggregates the mean lifetime of the 2_1^+ state and the partial lifetimes of all states decaying to it. Therefore, the intensities of the I_{sh} and I_{un} components of the 727-keV transition derived from the spectra in Fig. 4.4 have to be corrected for the effects of the transitions feeding the 2_1^+ state. Due to the reaction mechanism it is justified to consider that slow feeding contributions to the effective lifetimes of excited states of ^{212}Po can originate only from discrete decays of higher-lying states, as suggested in Ref. [22]. The partial level scheme representing the known transitions directly populating the 2_1^+ state of ^{212}Po [11, 22] is shown in Fig. 4.5.

Amongst them only the 405-keV $4_1^+ \rightarrow 2_1^+$ transition can be clearly observed
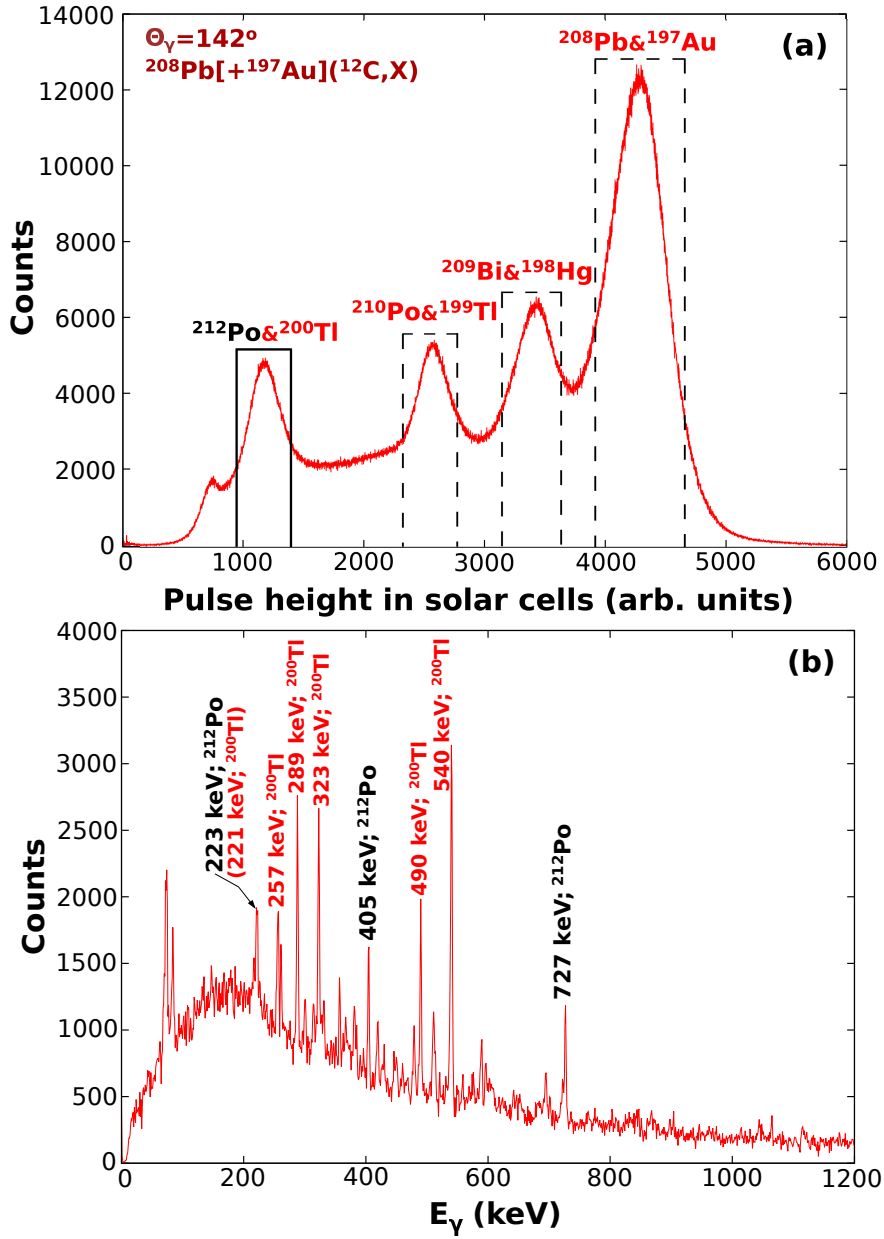
Figure 4.3: (a) The projection of the particle-γ matrix obtained at plunger distance D=43 μm by coincident detection of charged particles in the solar-cell array and a γ ray at a polar angle $\Theta_\gamma = 142°$. The marked ranges represent parts of the particle spectrum found to be in coincidence with the γ rays from the indicated nuclei. (b) The γ-ray spectrum in coincidence with the group of particles indicated as "^{212}Po & ^{200}Tl" in panel (a).
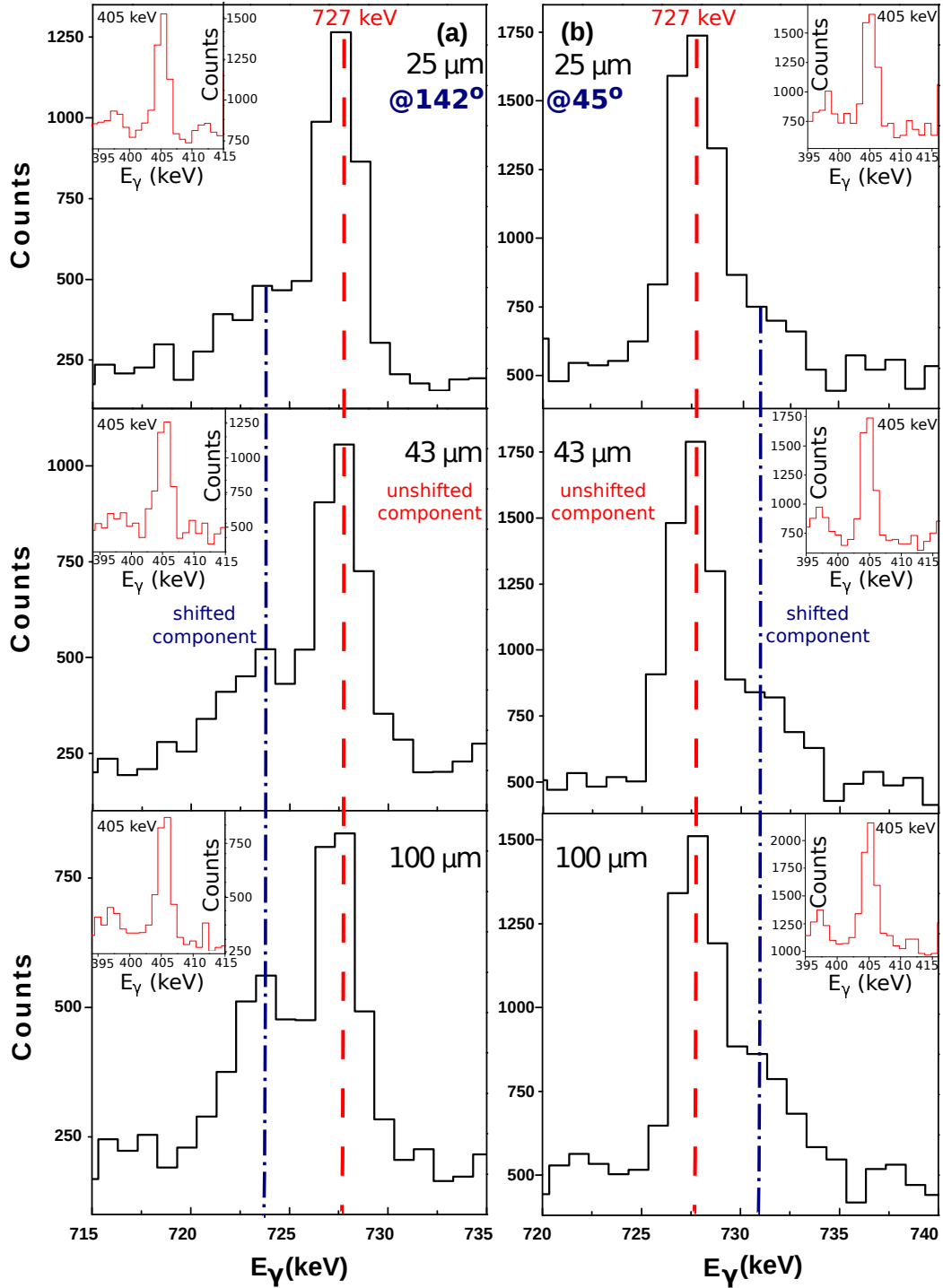
Figure 4.4: Unshifted and shifted components of the 727-keV ($2_1^+ \rightarrow 0_1^+$) transition observed at backward angles (a) and at forward angles (b) for three different target-to-stopper distances: 25 μm, 43 μm, 100 μm. The dot-dashed lines (blue) represent the positions of the Doppler-shifted peak; the dashed lines (red) represent the unshifted peak positions. In the upper corners are shown the peaks of the 405-keV ($4_1^+ \rightarrow 2_1^+$) transition at the same detector angle and distance as those for the $2_1^+ \rightarrow 0_1^+$ transition.

Figure 4.5: Partial level scheme of ^{212}Po showing the excited states which feed the first excited 2^+ state directly. The thicknesses of the arrows are proportional to the observed γ-ray intensities.
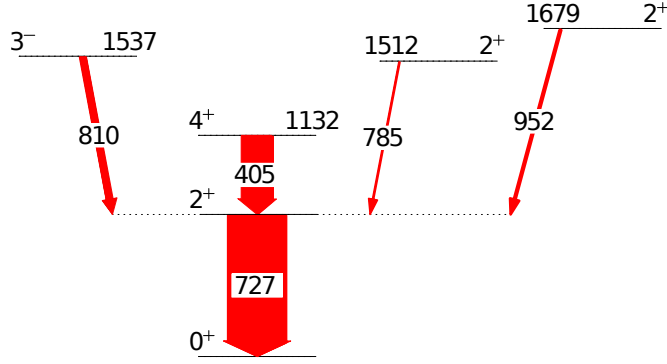
and its intensity can unambigously be determined in our data (cf. Fig. 4.3(b)). The reason for this is that the particle gated spectra in Fig. 4.3 is dominated by γ rays from ^{200}Tl produced by a transfer reaction in the backing or in the plunger stopper. In order to estimate the relative contributions of the feeding transitions (cf. Fig. 4.5) to the intensity of the 727-keV $(2_1^+ \to 0_1^+)$ transition we have used the data from our DSAM experiment in the previous chapter. In that experiment the same transfer reaction was utilized and as a result the same relative population of excited states of ^{212}Po could be expected. Indeed, the data from the previous experiment show that the intensity ratio $I_\gamma(405 \text{ keV}; 4_1^+ \to 2_1^+)/I_\gamma(727 \text{ keV}; 2_1^+ \to 0_1^+)$ is $55.0(8)/100.0(5)$ while $54(9)/100(4)$ is measured in the present experiment. This consistency allows to conclude that the intensities for the other transition have to be identical for both experiments as well. Therefore, we have estimated that 75% of the feeding of the 2_1^+ state comes from the states depicted in Fig. 4.5 as follows: 55% from the decay of the 4_1^+ state at 1132 keV excitation energy, 4% from the decay of the 2_2^+ state at 1512 keV, 6% from the decay of the 2_3^+ state at 1679 keV, and 10% from the decay of the 3_1^- state at 1537 keV. Since no other γ rays that feed the 2_1^+ state are observed up to date, the remaining 25% of the intensity of the 727-keV transition is considered to originate from a direct population of the 2_1^+ state.

In the previous chapter it was shown that the lifetimes of the $2_{2,3}^+$ states of ^{212}Po are below 1 ps which means that they contribute only to the fast feeding of the 2_1^+ state. The lifetime of the 3^- state at 1537 keV is not known and cannot be determined from any of the available data sets. However, an $E1$ strength of about 1 mW.u. for the 810-keV transition (cf. Fig. 4.5) leads to a $\tau(3_1^-) \approx 0.5$ ps. Therefore, in order to simplify the discussion at this moment we assume that its lifetime is sufficiently short so that it decays only in flight. Nevertheless, the influence of the feeding from the 3^- state on the $\tau(2_1^+)$ will be discussed later. Under the above assumption the only essential feeder to the 2_1^+ state remains the 405-keV transition which depopulates the 4_1^+ state in ^{212}Po (cf. Fig. 4.5). It is expected that the 4_1^+ state has a long lifetime of about 140 ps, or longer (see Table 3.2). Indeed, as it can be seen from the insets in Fig. 4.4 the 405-keV transition has only a stopped component for all plunger distances, *i.e.* the

decay of the 4_1^+ state contributes only to the stopped component of the 727-keV transition. Hence, that extra contribution to the stopped component of the 727-keV transition has to be eliminated. In our analysis this was achieved by subtracting the efficiency-corrected number of counts in the 405-keV line out of the efficiency-corrected number of counts in the stopped component of the 727-keV transition (cf. Fig. 4.4). Under the considerations above, all other transitions feeding the 2_1^+ state (cf. Fig. 4.5) comes from short-lived states ($\tau <$ 0.5 ps). Hence, the intensities of the shifted components of the 727-keV transition being directly determined from the particle-gated spectra are not affected by the feeding transitions and consequently are related only to the lifetime of the 2_1^+ state of ^{212}Po.

It needs to be stressed that both I_{un} and I_{sh} as extracted by the procedure described above are natively bound to the fast feedings of the 2_1^+ state, including one directly from the reaction. In this respect, they can be considered as effectively derived from γ-ray spectra in coincidence with the shifted components of all transitions directly feeding the state of interest. Therefore, they can be used to determine the lifetime of the 2_1^+ state with the DDCM, $i.e.$ they can be used directly in Eq. (4.8).

To proceed with the DDCM analysis the mean velocity of the recoiling nuclei $\langle v \rangle$ has to be known. In order to make a realistic estimate of the mean velocity of the recoiling nuclei we have calculated the average drifting time of the recoiling nuclei in vacuum. The calculations are based on Monte Carlo simulations which account for all relevant stopping and straggling processes of the beam and the recoiling nuclei in the target, the experimental geometry, and the restrictions on the reaction kinematics imposed by the solar cell array. The simulations were carried out with the program APCAD [53,54]. The approach used for the slowing-down process was described in details in the previous chapter. Taking into account the reaction conditions such as beam energy, backing and target thickness, and restrictions on the reaction kinematics imposed by the solar cells array, the ion drift times for all target-to-stopper distances were calculated from the simulated distributions and averaged over distances. An example of these distributions, for distance – 43μm, is given in Fig. 4.6. The mean drift time for this target-to-stopper distance is simulated to be t_{drift}=19.0(27) ps, which translates to a mean velocity of $\langle v \rangle$ =0.75(11)%c. The averaged over all distances value for the mean velocity of the recoiling nuclei is calculated to be $\langle v \rangle$ =0.75(10)%c.

Parallel with the procedure described above, a second analysis for the velocity of the ions has been done. The value for the velocity was experimentally determined from the centroids of the shifted and the unshifted components of 727-keV transition using

$$E_\gamma = E_0(1 + \beta \cos\theta) \tag{4.9}$$

where E_γ is the energy of the centroid of the shifted component (when the nucleus decays in flight), E_0 is the centroid of the unshifted component (when the nucleus decays at rest), the velocity of the ion is $\beta = v/c$, and θ is the γ-detector angle with respect to the beam direction. The velocity of the recoiling nuclei was extracted to be $\langle v \rangle$ =0.72(5)%c, which is in agreement with the value calculated from the simulated ion drift time. For the final value for the velocity of the
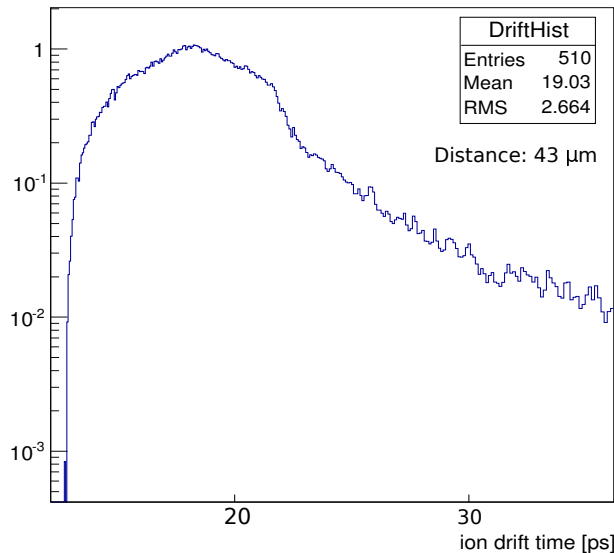
Figure 4.6: The simulated distribution of the drift time of the recoiling nuclei, for distance – 43μm. The value of t_{drift}=19.0(27) ps is used in order the mean velocity of the ions to be calculated.

nuclei we adopted the experimentally determined one since it is expected that that procedure is more accurate.

The DDCM analysis for the lifetime of the 2_1^+ state of ^{212}Po with $\langle v \rangle$ =0.72(5)%c and intensities (I_{un} and I_{sh}) extracted with the procedure described above is presented in Fig. 4.7 for forward and backward angles. The analysis results in a weighted mean value for the lifetime of the 2_1^+ state of 21.8(19) ps.

It has to be noted that the only assumption in the derivation of the above result which is not directly supported by experimental observations, is that the feeding from the 3_1^- state is fast (cf. Fig. 4.5). To investigate the influence of this feeding to the lifetime of the 2_1^+ state further, we have also considered the alternative limit, $i.e.$ we assume that the feeding from the 3_1^- state is very slow and contributes only to the unshifted component of the 727-keV transition. In this case, besides the intensity of the 405-keV transition, the intensity of the unshifted component of the 727-keV transition has to be reduced by additional 10% which accounts for the intensity of the 810-keV transition ($3_1^- \rightarrow 2_1^+$, cf. Fig. 4.5). This alternative approach reduces the deduced lifetime of the 2_1^+ to 19.2(18) ps. For the final value for the lifetime of the 2_1^+ state we conservatively adopt the average value between the two limits which is:

$$\tau(2_1^+, E_x = 727 \text{ keV}) = 20.5(26) \text{ ps.} \tag{4.10}$$

Taking into account the known electron conversion coefficient for the $2_1^+ \rightarrow 0_1^+$ transition of ^{212}Po [11] and the α-branching ratio of 0.033 [22], the newly derived lifetime of the 2_1^+ state translates to absolute transition strength $B(E2; 2_1^+ \rightarrow 0_1^+) = 193(24)$ e^{2}fm^4 = 2.6(3) Wu.
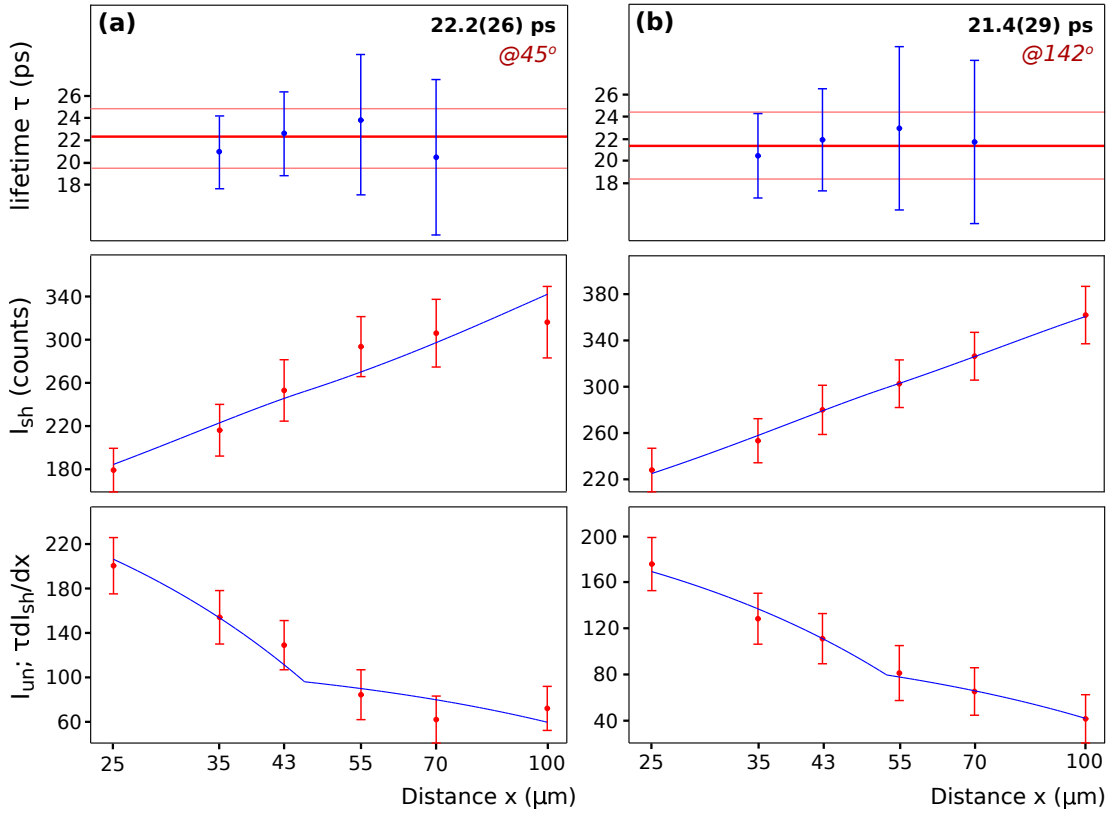
Figure 4.7: The lifetime of the first excited 2^+ state of ^{212}Po determined at forward (left) and backward angles (right). The middle panels show the shifted intensities at different distances. Continuous curves are fitted through the points to calculate the derivative. In the bottom panels, curves that represent the product between the time derivatives of the shifted intensities and the lifetime of the level are compared with the experimental unshifted intensities. Out of this comparison, the lifetimes corresponding to each distance in the region of sensitivity are extracted, as seen in the upper panel. The horizontal lines represent the weighted mean values.

4.3 Interpretation of the results - unexpected low collectivity of the 2_1^+ state

The measured $B(E2; 2_1^+ \rightarrow 0_1^+)$ value of 2.6(3) W.u. indicates an extremely low collectivity in the structure of the 2_1^+ state of ^{212}Po. Qualitatively, a low absolute transition strength from the 2_1^+ state in ^{212}Po can be expected in the framework of a single-j shell model since the wave function of the 2_1^+ state is expected to be neutron dominated as one can see in the previous chapter (3.3.1). Even in this case (see Tab. 3.2), the experimental value is also more than a factor of 2 smaller than the calculated one in the framework of a single-j shell model. Then a plausible explanation for the discrepancy between the predicted and the measured $B(E2; 2_1^+ \rightarrow 0_1^+)$ values could be sought in the choice of effective charges. In our calculations the effective proton and neutron charges in the $E2$ transition operator were determined from the measured $B(E2; 8_1^+ \rightarrow 6_1^+)$ values for ^{210}Pb and ^{210}Po. As it can be seen, the $B(E2)$ values for the decays of the 8_1^+ and the 6_1^+ states are reasonably well reproduced by the model approach while the experimental $B(E2; 2_1^+ \rightarrow 0_1^+)$ value is significantly overestimated (cf. Tab. 3.2).

Another approach is to determine the effective charges from the measured $B(E2; 2_1^+ \rightarrow 0_1^+)$ values for ^{210}Pb and ^{210}Po. There is information in the literature for these transition probabilities [57] but in the case for ^{210}Po, it is not very reliable. We will address this issue in the next chapter where the $B(E2; 2_1^+ \rightarrow 0_1^+)$ value for ^{210}Po is revised and continue with these theoretical calculations after determining the new $B(E2; 2_1^+ \rightarrow 0_1^+)$ value for ^{210}Po.

Chapter 5

The revised $B(E2; 2_1^+ \to 0_1^+)$ value in the nucleus ^{210}Po

The adopted $B(E2; 2_1^+ \to 0_1^+)$ value for ^{210}Po is determined from the cross-section for populating the 2_1^+ state in ^{210}Po measured in inelastic scattering of deuterons and protons [63]. Large-scale shell-model studies on ^{210}Po using realistic interactions [64,65] reproduce well the energies of the yrast 2^+, 4^+, 6^+, and 8^+ levels as can be seen in Fig. 5.1. The calculated wave functions in the framework of shell model show that the dominant component of the yrast states is the $(\pi h_{9/2})^2$ configuration, corroborating the expectation that they belong to the seniority $\upsilon = 2$ multiplet. The $E2$ strengths for the transitions between the 4^+, 6^+ and 8^+ states are also almost perfectly reproduced (cf. Table VII in Ref. [64] and Table III in Ref. [65]). However, in both studies [64,65] the $B(E2; 2_1^+ \to 0_1^+)$ value is overestimated by a factor of six. Such a significant discrepancy between the shell-model calculations and the data is an indication for either an inaccurate experimental value [64,65] or for deficiencies in the model, as suggested in Ref. [65]. This has motivated us to re-evaluate the lifetime of the 2_1^+ state of ^{210}Po using data from our DSAM experiment, namely the one obtained with the ^{208}Pb(^{12}C,^{10}Be)^{210}Po reaction. The set-up of this experiment is described in details in chapter 3.

5.1 Data analysis

A projection of the particle-γ matrix obtained with γ-ray detection at 142.3° is shown in Fig. 5.2(a). The γ rays in coincidence with the group of particles indicated as "^{210}Po" in Fig. 5.2(a) are shown in Fig. 5.2(b). This spectrum is dominated by the 1181-keV and the 245-keV lines which are the γ-ray transitions depopulating the first two yrast states of ^{210}Po [66] (cf. Fig. 5.1). Besides some contaminants from ^{211}Po (which are shown in purple), all other γ rays in the spectrum in Fig. 5.2(b) originate from the decay of excited states in ^{210}Po. Moreover, the 1181-, 2290-, and 1205-keV γ-ray lines show well-pronounced Doppler shapes which allow us to extract the lifetimes of the 2_1^+, the 2_2^+ and the 3_1^- states in ^{210}Po, respectively.

   To perform the line-shape analysis we used again the software package AP-CAD. As it was mentioned above the analysis accounts for the response of the
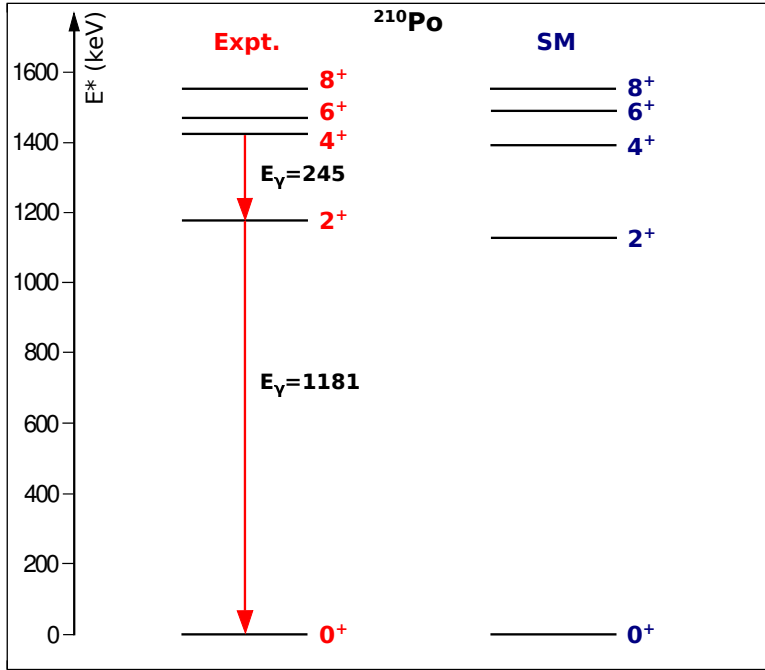
Figure 5.1: Experimental and calculated yrast states of ^{210}Po. The calculated shell-model levels are taken from Ref. [64].

HPGe detectors, for the experimental geometry, for the restrictions on the reaction kinematics imposed by the solar-cell array and for the feeding history. A partial level scheme representing the known transitions directly populating the 2_1^+ state of ^{210}Po [66] is shown in Fig. 5.3.

The lifetimes of the 2_2^+ state at 2290 keV and 3_1^- state at 2387 keV were extracted from the line shapes of the 2290-keV $(2_2^+ \rightarrow 0_1^+)$ and the 1205-keV $(3_1^- \rightarrow 2_1^+)$ transitions in particle-gated spectra, respectively. These spectra are, in fact, γ-ray singles spectra which, in principal, only contain information for the effective lifetimes. However, due to the reaction mechanism it is justified to consider that slow feeding contributions to the effective lifetimes of excited states of ^{210}Po can originate only from discrete decays of higher-lying states, as suggested in Ref. [22]. The $\gamma - \gamma$ coincidence data show that the 1205-keV transition is in coincidence with the 1181-keV $(2_1^+ \rightarrow 0_1^+)$ transition only, while the 2290-keV $(2_2^+ \rightarrow 0_1^+)$ transition is not present in the coincidence data. This observation indicates that the 2_2^+ and the 3_1^- states are directly populated in the transfer reaction. Therefore only fast feeding $(\tau_{feeding} \leq 10 \text{ fs})$ was introduced in the fits of their line shapes. The fits are presented in Fig. 5.4 and the extracted lifetimes are summarized in Table 5.1.

The lifetime of the first excited 2^+ state in ^{210}Po was obtained from the line shape of the 1181-keV $(2_1^+ \rightarrow 0_1^+)$ transition. Using the $\gamma - \gamma$ and the γ-particle coincidence data from our experiment, and the known branching ratios [66] we have estimated that 38% of the feeding of the 2_1^+ state originates from the states depicted in Fig. 5.3. The $\gamma - \gamma$ and the γ-particle coincidence data were used to estimate that the contributions of the 245-keV and the 1205-keV transitions account for 20% and 16%, respectively (cf. Fig. 5.3). We have not observed
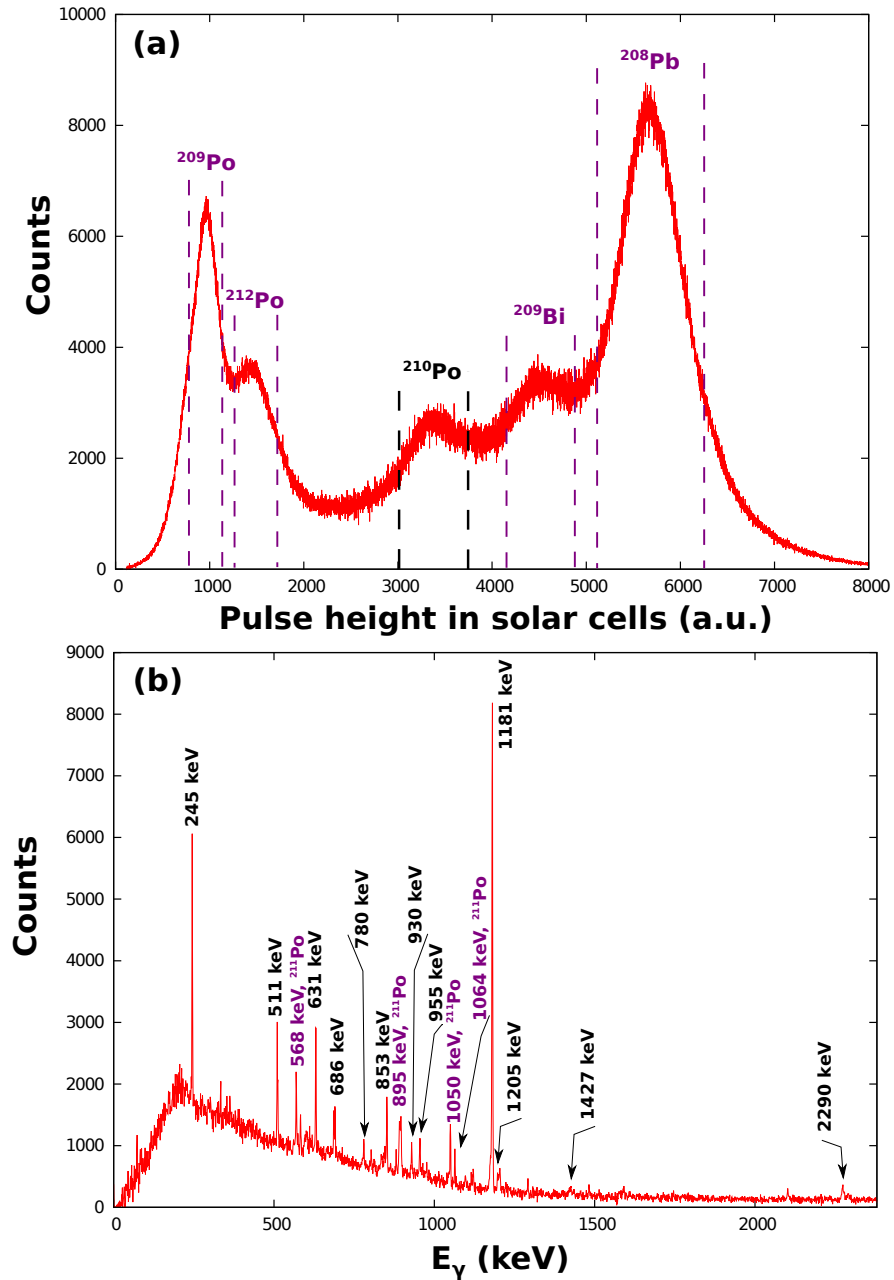
Figure 5.2: (a) The projection of the particle-γ matrix obtained by coincidence detection of charged particles in the solar-cell array and a γ ray at $\Theta_\gamma = 142°$ polar angle. The vertical dashed lines represent parts of the particle spectrum found to be in coincidence with γ rays from the indicated nuclei. (b) The γ-ray spectrum in coincidence with the group of particles indicated as "^{210}Po" in panel (a).
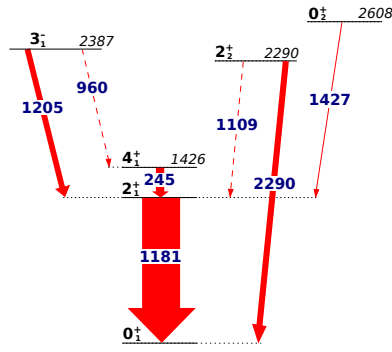
Figure 5.3: Partial level scheme of ^{210}Po showing the excited states which feed the first 2^+ state directly. The thicknesses of the arrows are proportional to the observed γ-ray intensities. The transitions not observed in our data are presented with dashed arrows.

the 1109-keV ($2_2^+ \rightarrow 2_1^+$) transition in our data. However, the 2290-keV ($2_2^+ \rightarrow 0_1^+$) transition is clearly visible in the γ-particle data (cf. Fig. 5.2(b)) which in combination with the known branching ratio for the decay of the 2_2^+ state [66] allowed us to estimate that the feeding to the 2_1^+ state via the 1109-keV transition is 2%.

The lifetimes of the 2_2^+ and the 3_1^- state (cf. Table 5.1) and their influence on the line shape of the 1181-keV transition were taken into account by the fitting procedure for the lifetime of the 2_1^+ state. A special care was taken to account for the impact of the 245-keV ($4_1^+ \rightarrow 2_1^+$) transition. The 4_1^+ state in ^{210}Po is a long-lived state with lifetime $\tau = 2.21(10)$ ns [67]. Consequently, it always decays at rest in the present experiment. The same is valid for the decays of the 6_1^+ and the 8_1^+ states (cf. Fig. 5.1). Their lifetimes are even longer than the one for the 4_1^+ state [67]. It has to be noted, that although we have not observed γ-ray transitions from the decays of the 6_1^+ and the 8_1^+ states, the population of these states in the present experiment cannot be excluded and their decay could potentially contribute to the yield of the 245-keV transition in the cascade $8_1^+ \rightarrow 6_1^+ \rightarrow 4_1^+ \rightarrow 2_1^+$ (cf. Fig. 5.1). However, due to the isomeric nature of the 4_1^+, the 6_1^+ and the 8_1^+ states the overall effect of their decays is that the 245-keV ($4_1^+ \rightarrow 2_1^+$) transition is always emitted at rest in the present experiment. Indeed, as can be seen from the insets in Fig. 5.5 the 245-keV γ-ray line show no indication of Doppler-shifted components in its shape. Hence, when the 2_1^+ state is fed by the $4_1^+ \rightarrow 2_1^+$ transition it also always decays at rest which gives extra counts into the fully stopped component of the 1181-keV transition. In order to extract correctly the lifetime of the first 2^+ state of ^{210}Po by means of the Doppler-shift attenuation method, the contribution of the γ rays coming from the 245-keV transition to the fully stopped component of the 1181-keV transition has to be eliminated. The efficiency corrected number of counts in the 245-keV line are subtracted from the efficiency corrected number of counts in the stopped component of the 1181-keV transition. That procedure could be automatically carried out with APCAD by simultaneously fitting the 1181- and the 245-keV lines.

In addition, the $\gamma - \gamma$ coincidence data indicate the presence of 1427-keV
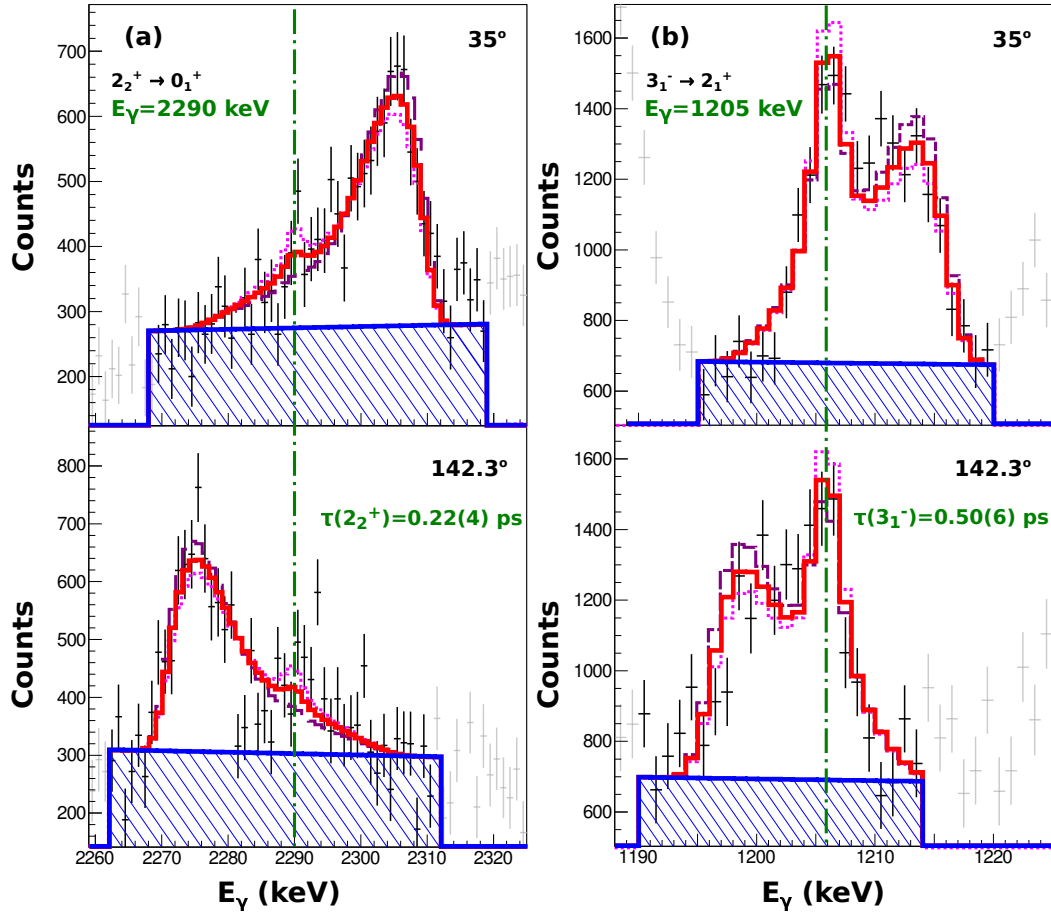
Figure 5.4: An example of line-shape fits of the 2290.1-keV $(2_2^+ \rightarrow 0_1^+)$ (a) and the 1205.4-keV $(3_1^- \rightarrow 2_1^+)$ (b) transitions. The crossed (blue) areas show the background regions. The solid (red) lines represent the fits corresponding to the adopted lifetimes. The vertical dash-dotted (green) lines show the position of the unshifted peaks. The dashed (violet) and the dotted (pink) lines represent the fits with $\tau - \sigma$ and $\tau + \sigma$, respectively.
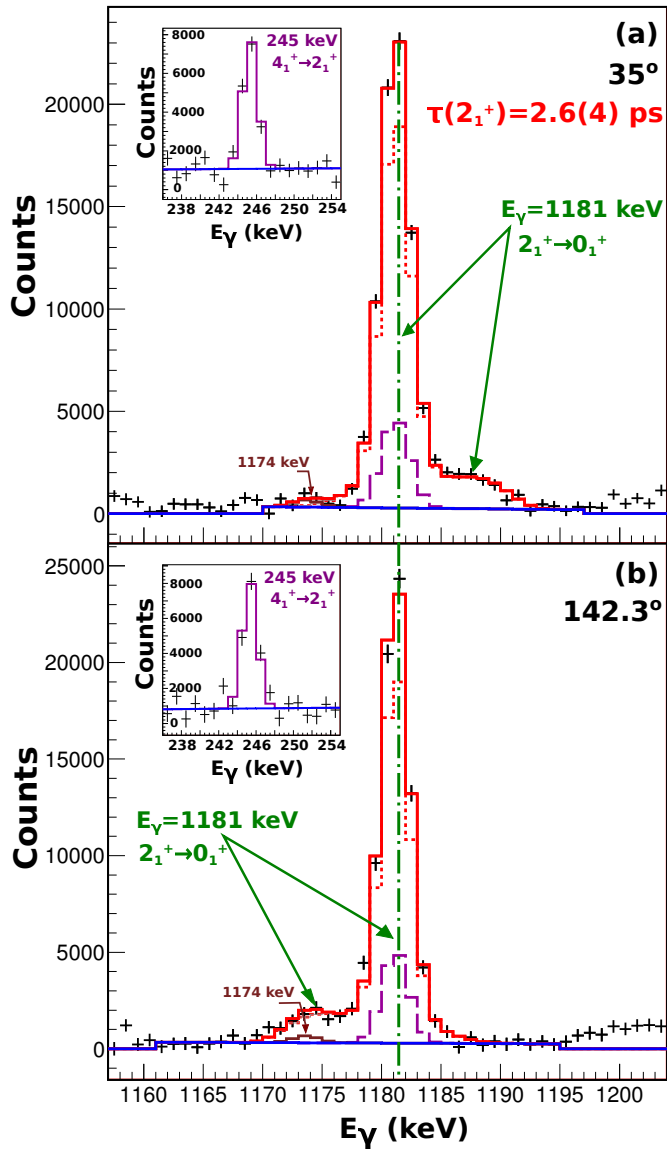
Figure 5.5: Simultaneous line-shape fits of the 1181-keV ($2_1^+ \rightarrow 0_1^+$) transition observed at forward (a) and at backward (b) angles. The solid (red) line represents the total fit. The 1181-keV line is fitted simultaneously with the 245-keV ($4_1^+ \rightarrow 2_1^+$) line which is always emitted from a stopped nucleus (the insets). The dotted and dashed lines represent the individual contributions of 1181-keV (red) and 245-keV (purple) lines, respectively, to the total fit. An unidentified stopped contaminant with $E_\gamma = 1174$ keV is taken into account (brown).

Table 5.1: Properties of the three investigated low-lying states of ^{210}Po and γ-ray transitions originating from their decays. Denoted are: the excitation energies (E_{level}); the spin and parity of the initial levels (J^{π}) and of the final levels (J^{π}_{final}); the γ-ray energies (E_{γ}); the relative intensities (I_{γ}); the multipole mixing ratios (δ) of the γ-ray transitions; the lifetimes of the states; the absolute transition strengths. For calculating the absolute transition strengths the total electron conversion coefficients α from Ref. [12] were used.

E_{level} (keV)	J^{π}	J^{π}_{final}	E_{γ} (keV)	I_{γ} [a] %	δ [b]	τ (ps)	Transition strength [c] $J^{\pi} \to J^{\pi}_{final}$
1181	2^+_1	0^+_1	1181	100		2.6(4)	$B(E2)$=136(21)
2290	2^+_2	0^+_1	2290	100(2)		0.22(4)	$B(E2)$=53(11)
		2^+_1	1109	11.2(11)	0.61(31)		$B(M1)$=0.014(7)
							$B(E2)$=60(29)
2387	3^-_1	0^+_1	2387	1.0(3)		0.50(6)	$B(E3)$=70(31)$\times 10^3$
		2^+_1	1205	100.0(15)			$B(E1)$=0.64(9)$\times 10^{-3}$
		4^+_1	960	11.3(6)			$B(E1)$=0.14(3)$\times 10^{-3}$

[a]From Ref. [66].

[b]From Ref. [12].

[c]$B(E1)$ values are given in e^2fm^2, $B(E2)$ values are given in e^2fm^4 (1 W.u.=74.15 e^2fm^4), $B(E3)$ value is given in e^2fm^6, and $B(M1)$ value is given in μ_N^2.

transition that connects the 0^+_2 state at 2608 keV and the 2^+_1 state. However, this is an extremely weak transition which accounts for less than 1% of the total population of the 2^+_1 state and practically, has no impact on the lifetime of the 2^+_1 state. Therefore, besides the influence of the feeding from the 4^+_1, the 2^+_2 and the 3^-_1 states, only fast feeding ($\tau_{feeding} \leq 10$ fs) was considered in the fit of the line shape of 1181-keV transition. Under this assumption, the final value of the lifetime of the 2^+_1 is extracted from a simultaneous line-shape fit of the 1181-keV transition observed at forward and backward angles (see Fig. 5.5) and presented in Table 5.1.

5.2 Interpretation of the results

The lifetimes from the present study, together with the available spectroscopic information and the resulting transition strengths, are summarized in Table 5.1. The lifetime for the 3^-_1 state in ^{210}Po is in a good agreement with the estimated value from Ref. [63]. The lifetime of the 2^+_2 state is measured for the first time. The new value for the 2^+_1 state is about a factor of three shorter than the adopted one [12]. The latter is deduced from a relative cross-section measurement in a (d, d') scattering experiment [63]. It has to be noted, however, that the new value is in a better agreement with the lifetime resulting from the cross-section for (p, p') scattering reported in the same study [63]. On the other hand, the value from the present study is obtained by a model-independent technique and free of the systematic uncertainties inherent to cross-section analysis.

The shorter lifetime of the 2_1^+ state leads to $B(E2; 2_1^+ \rightarrow 0_1^+) = 1.83(28)$ W.u. which is about three times larger than the adopted value [12,63]. However, this is not sufficient to compensate for the discrepancy between the experimental value and the estimations within the pure seniority scheme [68] or the shell model result (cf. Table VII in Ref. [64] and Table III in Ref. [65]) which remain two times larger than the experimental value. At this point the discrepancy cannot be explained any longer as being due to experimental uncertainties, the alternative that it results from the deficiencies of shell model [65] seems more likely. In Ref. [65] the flaw is attributed to the neglect of ph excitations of the ^{208}Pb core which strongly influence the $J^\pi = 2^+$ states [69].

It is also interesting to check whether the problem is specific for shell models and whether other theoretical approaches can do better in describing the properties of low-lying states of ^{210}Po. For this purpose we have performed Quasi-particle Phonon Model (QPM) calculations [70] for ^{210}Po.

5.3 Quasi-particle Phonon Model (QPM) calculations for the nucleus ^{210}Po

The Quasi-particle Phonon Model is a microscopic approach extending the quasi-particle random-phase approximation (QRPA) to a multiphonon basis [71]. In the QPM, a Hamiltonian of general separable form is treated in a microscopic multiphonon basis. It is therefore able to describe the anharmonic features of collective modes as well as the multiphonon states. The method can be put in close correspondence with the proton-neutron interacting boson model. By associating the microscopic isoscalar and isovector quadrupole phonons with proton-neutron symmetric and mixed-symmetry quadrupole bosons, respectively, the microscopic states can be classified, just as in the algebraic model, according to their phonon content and their symmetry. Due to its flexibility, the method can be implemented numerically for systematic studies of spectroscopic properties throughout entire regions of vibrational nuclei.

The model incorporates a two-body Hamiltonian, which itself is composed of several multipole-multipole potentials, allowing the QPM to cover a large configuration space. A short summary of the basic principles, based on [71], is presented in the following lines [72]. The QPM works with a Hamiltonian of the form

$$H = H_{sp} + V_{pair} + V_M^{ph} + V_{SM}^{ph} + V_M^{pp} \tag{5.1}$$

where H_{sp} is a single-particle Hamiltonian, including a mean-field Wood-Saxon potential, V_{pair} is the monopole pairing, V_M^{ph} and V_{SM}^{ph} include multipole and spin-multipole interactions of particles and holes, while V_M^{pp} represents the multipole interaction of particles. The definitions of the potentials can be found in [71].

Based on the particle and hole generation operators $a_q^\dagger$ and a_q, the quasiparticle generation and elimination operators $\alpha_q^\dagger$ and α_q are derived. The separable Hamiltonian is then used to generate the QRPA phonons via

$$Q_\lambda^\dagger = \frac{1}{2}\sum_{qq'}\{\psi_{qq'}^\lambda[\alpha_q^\dagger \alpha_{q'}^\dagger]_\lambda - \varphi_{qq'}^\lambda[\alpha_{q'}\alpha_q]_{\bar\lambda}\} \tag{5.2}$$

The amplitudes $\psi_{qq'}^\lambda$ and $\varphi_{qq'}^\lambda$ are required to fulfill the conditions

$$\frac{1}{2}\sum_{qq'}[\psi_{qq'}^\lambda \psi_{qq'}^{\lambda'} - \varphi_{qq'}^\lambda \varphi_{qq'}^{\lambda'}] = \delta_{\lambda\lambda'} \tag{5.3}$$

The QRPA phonons generated this way allow for expressing the Hamiltonian of quasiparticle separable form by phonons via

$$H_{QPM} = \sum_\lambda \omega_\lambda Q_\lambda^\dagger Q_\lambda + H_{vq} \tag{5.4}$$

where $\omega_\lambda Q$ is the QRPA phonon energy and H_{vq} is a phonon coupling part. The Hamiltonian transformed into the phonon form is diagonalized in a space spanned by states composed of one, two and three QRPA phonons. The wave functions are then given by

$$\Psi_{\nu JM} = \sum_i R_i^{\nu J} Q_{iJM}^\dagger |0\rangle + \sum_{\lambda_1\lambda_2} P_{\lambda_1\lambda_2}^{(\nu J)}[Q_{\lambda_1}^\dagger \otimes Q_{\lambda_2}^\dagger]_{JM}|0\rangle +$$
$$+ \sum_{\lambda_1\lambda_2}^{\lambda_3 I} T_{\lambda_1\lambda_2\lambda_3}^{(\nu J)}[[Q_{\lambda_1}^\dagger \otimes Q_{\lambda_2}^\dagger]_I \otimes Q_{\lambda_3}^\dagger]_{JM}|0\rangle \tag{5.5}$$

They have to be normalized and antisymmetrized according to a particular procedure outlined in Ref. [71].

In the QPM, one-body transition operators $\mathfrak{M}(\sigma\lambda)$ can be separated into two pieces, leading to the expression

$$\mathfrak{M}(\sigma\lambda) = \mathscr{M}_{ph}(\sigma\lambda) + \mathscr{M}_{sc}(\sigma\lambda) \tag{5.6}$$

The first term connects states differing by one phonon. It is the leading term and is responsible for the boson-allowed transitions. It is given by

$$\mathscr{M}_{ph}(\sigma\lambda\mu) = \frac{1}{\sqrt{2\lambda+1}}\sum_{qq'}\langle q||\mathfrak{M}(\sigma\lambda)||q'\rangle(u_q v_{q'} \pm v_q u_{q'})(\Psi_{qq'}^\lambda + \Phi_{qq'}^\lambda)(Q_\lambda^\dagger + Q_{\bar\lambda}) \tag{5.7}$$

The second term is the quasiparticle scattering term, which is given by

$$\mathscr{M}_{sc}(\sigma\lambda) = \frac{1}{\sqrt{2\lambda+1}}\sum_{qq'}\langle q||\mathfrak{M}(\sigma\lambda)||q'\rangle(u_q u_{q'} \mp u_q u_{q'})[\alpha_q^\dagger \times \alpha_{q'}]_\lambda \tag{5.8}$$

This term links states with the same number of phonons, or with phonon counts differing by two, and is responsible for the boson-forbidden transitions.

Usually, the problem in the application of the QPM is the determination of the parameters. The parameters of the Wood-Saxon potential are chosen to

Table 5.2: Results from the QPM calculations for excitation energies of ^{210}Po in comparison with the experimental data. The values are given in MeV.

J^π	2_1^+	4_1^+	6_1^+	8_1^+	2_2^+	3^-
Expt.	1.18	1.43	1.47	1.56	2.29	2.39
QPM	1.10	1.16	1.20	1.21	2.05	2.61

resemble single-particle spectra. The single-particle space includes shells below and bound states above the Fermi energy, to maximize the energy range available for investigation of nuclear structure. In general, sets of parameters are always determined for a particular mass region, and used for calculations of the full energy range. The details about the calculations which we have done for ^{210}Po are presented bellow.

In our calculations we have used the Woods-Saxon potential for the mean field with the parameters presented in Ref. [73]. The single-particle space includes all shells from the potential bottom to quasibound states with narrow widths. The single-particle energies of the levels near the Fermi surface are taken from Ref. [74], where they have been adjusted to reproduce experimental energies of low-lying levels of four odd-mass neighbouring nuclei to ^{208}Pb in a calculation with the interactions between quasiparticles and phonons accounted for. The strength of the monopole pairing interaction for protons in ^{210}Po was adjusted to the corresponding even/odd mass differences. Because of the large single-particle model space no effective charges were used for calculating the $E1$, $E2$, and $E3$ transition strengths. The spin-gyromagnetic quenching factor used to calculate the $M1$ transition strengths is $g_s^{\text{eff}} = 0.8 g_s^{\text{free}}$. Excitation modes of even-even nuclei (both collective and almost two-quasi-particle ones) are treated in the QPM in terms of phonons. Their excitation energies and internal fermion structure is obtained from solving Quasi-particle Random-Phase Approximation (QRPA) equations. The model uses a separable form of the residual interaction. In the present studies we have used Bohr-Mottelson form factor of the residual force as a derivative of the mean-field potential. The strength of the isoscalar residual interaction, the same for all multipoles, has been adjusted to the experimental $B(E2, 2_1^+ \rightarrow 0_{g.s.})$ value in ^{210}Po. The calculations have been performed on the basis of interacting one-, two-, and three-phonon configurations. The phonons of the 2^+, 3^-, 4^+, 6^+, and 8^+ multipolarities have been involved. Complex (two- and three-phonon) configurations have been built up from all possible combinations of these phonons. The basis has been truncated above 6 MeV, 8 MeV, and 10 MeV for one-, two-, and three-phonon components, respectively.

The results from the calculations are presented and compared to the experimental data in Table 5.2 and Table 5.3. The energies of the states of interest are reasonably well reproduced but the lowest 4^+, 6^+, and 8^+ states are practically degenerate in energy because of their almost pure $\pi\{(1h_{9/2})^2\}$ nature. It has to be noted that in the chosen approach to fix the strength parameters to the electric strengths of the 2_1^+ state, the result for the energies of the states should be considered as a prediction of the model. In this respect, the agreement between the

Table 5.3: Results from the QPM calculations for the low-lying states of ^{210}Po in comparison with the experimental data.

J_i^π	Structure [a] %	J_f^π	Transition strength [b] Expt.	QPM
2_1^+	$97\%[2_1^+]_{RPA}$	0_1^+	$B(E2){=}136(21)$	$B(E2){=}135$ [c]
4_1^+	$99\%[4_1^+]_{RPA}$	2_1^+	$B(E2){=}331(13)$ [d]	$B(E2){=}41$
6_1^+	$99\%[6_1^+]_{RPA}$	4_1^+	$B(E2){=}227(5)$ [e]	$B(E2){=}28$
8_1^+	$99\%[8_1^+]_{RPA}$	6_1^+	$B(E2){=}83(3)$ [f]	$B(E2){=}11$
2_2^+	$1.2\%[2_1^+]_{RPA} +$ $+ 60.5\%[2_1^+ \otimes 2_1^+]_{RPA} +$ $+ 20.7\%[2_1^+ \otimes 4_1^+]_{RPA}$	0_1^+ 2_1^+ 2_1^+	$B(E2){=}53(11)$ $B(M1){=}0.014(7)$ $B(E2){=}60(29)$	$B(E2){=}3.4$ $B(M1){=}0.006$ $B(E2){=}80$
3^-	$95\%[3_1^-]_{RPA}$	0_1^+ 2_1^+ 4_1^+	$B(E3){=}70(31){\times}10^3$ $B(E1){=}0.64(9){\times}10^{-3}$ $B(E1){=}0.14(3){\times}10^{-3}$	$B(E3){=}70{\times}10^3$ $B(E1){=}0.83{\times}10^{-3}$ $B(E1){=}0.27{\times}10^{-3}$

[a]$[2_1^+]_{RPA}$ means the lowest in energy RPA phonon of the multipolarity 2^+, etc.

[b]$B(E1)$ values are given in e^2fm^2, $B(E2)$ values are given in e^2fm^4 (1 W.u.=74.15 e^2fm^4), $B(E3)$ value is given in e^2fm^6, and $B(M1)$ value is given in μ_N^2.

[c]The strength of the quadrupole isoscalar residual interaction has been adjusted to the experimental $B(E2, 2_1^+ \to 0_{g.s.})$ value in ^{210}Po.

[d]From Ref. [12].

[e]From Ref. [67].

[f]From Ref. [12].

experimental and the calculated energies for the 2_1^+ and the 3_1^- states allows to interpret them as one-quadrupole and one-octupole phonon states, respectively. The energies of the 4_1^+, 6_1^+, and 8_1^+ states are somewhat lower in the calculation than experimentally observed. It should be noted that the energy of the lowest two-quasiparticle configuration $\pi\{(1h_{9/2})^2\}$ is 1.211 MeV with the present quasiparticle spectrum. In general, the calculation predicts a rather pure one-phonon nature of the lowest 2^+, 4^+, 6^+ and 8^+ states.

The major discrepancy between the QPM calculations and the experimental data appears in the $E2$ transition strengths for the cascade $8_1^+ \rightarrow 6_1^+ \rightarrow 4_1^+$ (cf. Table 5.3). Overall, the model underestimates these values by a factor of 8. Since the corresponding states have a rather pure one-phonon nature, these transitions are determined by the $E2$ matrix elements $\langle [6_1^+]_{RPA}||E2||[8_1^+]_{RPA}\rangle$, etc. These matrix elements are much smaller as compared to the decays from two-phonon components $\langle [6_1^+]_{RPA}||E2||[2_1^+ \otimes 6_1^+]_{RPA}\rangle$, etc with an exchange of the $[2_1^+]_{RPA}$ phonon [75]. Experimental data definitely indicate strong admixture of two phonon components in the structure of the 4_1^+, 6_1^+, and 8_1^+ states which is not reproduced in the QPM calculations. The problem existing in the shell model description also appears in a different form in the present QPM calculations, namely both models are not capable of describing consistently the $E2$ transition strengths between the states in the $2_1^+ - 4_1^+ - 6_1^+ - 8_1^+$ yrast sequence. This may indicate that the ^{208}Pb core is soft as this softness strongly enhances the $1ph$ excitations, or facilitates mixing between the $2qp$ configurations.

Chapter 6

Low quadrupole collectivity in the nucleus ^{212}Po

Before continuing with more theoretical interpretation of our results now we would like to summarize the most important results about the degree of quadrupole collectivity in ^{212}Po presented up to this point. In section 3.3.1. the theoretical calculations based on the single-j shell model were presented in order to describe the properties of the low-lying states in ^{212}Po. It was shown that the energies for most of the states are well reproduced and the agreement between the experimental and the calculated transition strengths for the 2_2^+ and 2_3^+ excited states is qualitatively good. In section 4.3. was shown that the measured $B(E2; 2_1^+ \rightarrow 0_1^+)$ value in ^{212}Po is more than a factor of 2 smaller than the calculated one in the framework of the single-j shell model. It was suggested that an explanation for this discrepancy could be sought in the choice of effective charges. In our calculations the effective proton and neutron charges in the $E2$ transition operator were determined from the measured $B(E2; 8_1^+ \rightarrow 6_1^+)$ values for ^{210}Pb and ^{210}Po. Another approach is to determine the effective charges from the measured $B(E2; 2_1^+ \rightarrow 0_1^+)$ values for ^{210}Pb and ^{210}Po. For this purpose, in the previous chapter, we revised the $B(E2; 2_1^+ \rightarrow 0_1^+)$ value for ^{210}Po in order to have more reliable results. In the following section the results from shell model calculations for ^{212}Po incorporating the new $B(E2; 2_1^+ \rightarrow 0_1^+)$ value for ^{210}Po are presented.

6.1 Single-j shell model calculations with effective charges fixed to the $B(E2; 2_1^+ \rightarrow 0_1^+)$ values in ^{210}Po and ^{210}Pb

Using the measured $B(E2; 2_1^+ \rightarrow 0_1^+)$ values for ^{210}Pb [57] and ^{210}Po single-j shell model calculations were performed which leads to effective charges of e_ν=0.83e and e_π=1.09e. The results from these calculations are presented in Table 6.1 and in Fig. 6.1, labelled as SM2-gh. Not surprisingly, the calculated $B(E2; 2_1^+ \rightarrow 0_1^+)$ value for ^{212}Po is closer to our experimental one. It is also worth noting that such an improvement in the description of the $B(E2; 2_1^+ \rightarrow 0_1^+)$ value leads to a perfect agreement between the experimental and the calculated $B(E2; 2_2^+ \rightarrow 0_1^+)$

values (cf. Table 6.1). This, however, can be expected since the 2_2^+ state is the isovector partner of the 2_1^+ state, *i.e.* these two states of ^{212}Po have almost identical wave functions as the main difference between them is a phase factor (see section 3.3.1). On the other hand, the results for the transition strengths for the 8_1^+ and the 6_1^+ (cf. SM2-gh in Fig. 6.1) states are about a factor of two lower than the experimental ones. This analysis suggests that agreement between experimental and simple single-j shell model cannot be achieved for the $B(E2)$ rates by adjusting the effective charges.

Table 6.1: Comparison between the experimental and calculated (see text for details) properties of the low-lying states in ^{212}Po. The experimental $B(E2)$ values are from Refs. [12, 22], unless otherwise specified.

J_i^π	E_x (MeV)		J_f^π	$B(E2; J_i \to J_f)(\mathrm{e}^2\mathrm{fm}^4)$		
	Expt	SM-gh		Expt	SM1-gh[a]	SM2-gh[b]
2_1^+	0.727	0.690	0_1^+	193(24)[c]	464	271
4_1^+	1.132	1.081	2_1^+	—	535	313
6_1^+	1.355	1.261	4_1^+	293(83)	301	178
8_1^+	1.475	1.350	6_1^+	173(68)	103	62
2_2^+	1.512	1.363	0_1^+	29(4)[c]	59	27
			2_1^+	24(16)[c]	17	8

[a]With $e_\pi = 1.52e$ and $e_\nu = 1.04e$.
[b]With $e_\pi = 1.09e$ and $e_\nu = 0.83e$.
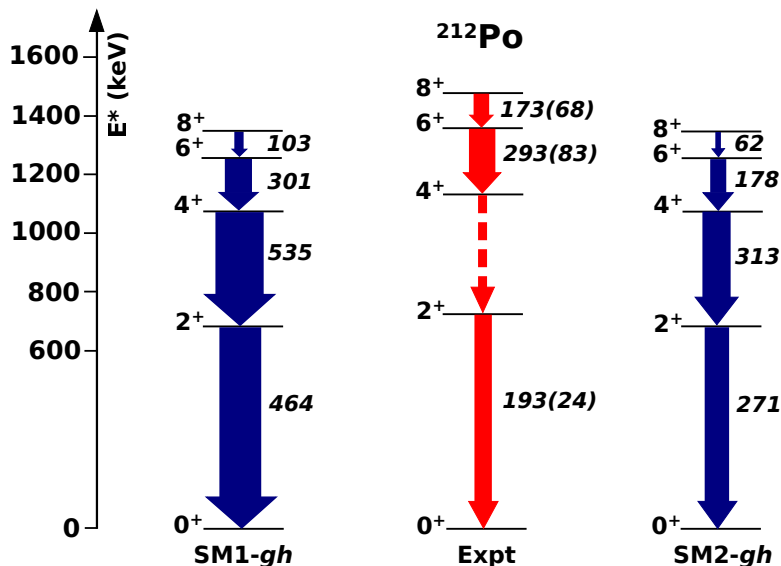[c]From the present work.

Figure 6.1: A graphical representation of the results from Table 6.1 for the single-j shell model calculations (SM1-gh and SM2-gh) for the low-lying states in ^{212}Po in comparison with experimental data (Expt). The thickness of the arrows is proportional to the $B(E2; 2_1^+ \to 0_1^+)$ values in e^{2}fm^4. The latter are also presented by the numbers next to the arrows.

Table 6.2: Comparison between the experimental and calculated (see text for details) properties of the yrast states in ^{210}Pb. The experimental excitation energies and $B(E2)$ values are from Ref. [57].

J_i^π	E_x (MeV)		J_f^π	$B(E2; J_i \to J_f)$(e^{2}fm^4)			
	Expt	SM		Expt	SM1-gh^a	SM2-gh^b	SM^b
2_1^+	0.800	0.837	0_1^+	105(30)	166	106	109
4_1^+	1.098	1.099	2_1^+	360(68)	191	121	144
6_1^+	1.195	1.191	4_1^+	158(60)	132	84	101
8_1^+	1.278	1.234	6_1^+	53(23)	53	34	43

^{a}With $e_\nu = 1.04e$.
^{b}With $e_\nu = 0.83e$.

Since the single-j shell model calculations use an empirical effective interaction derived from the spectra of ^{210}Pb, ^{210}Bi, and ^{210}Po, it is interesting to check whether the problem in the description of the $E2$ transition strengths between the yrast states of ^{212}Po is also present in ^{210}Pb and ^{210}Po. Results from the single-j shell-model calculations for these $B(E2)$ values in ^{210}Pb and ^{210}Po are presented in Tables 6.2 and 6.3 under the columns labelled SM1-gh and SM2-gh. The labelling of the columns reflects the approach in choosing the effective charges in the same way as in Table 6.1. The problem is clearly present for both nuclei – if the effective charges are fixed to the $B(E2; 8_1^+ \to 6_1^+)$ values (SM1-gh), the $B(E2; 2_1^+ \to 0_1^+)$ values are overestimated, otherwise, if the effective charges are fixed to the $B(E2; 2_1^+ \to 0_1^+)$ values (SM2-gh), the $B(E2; 8_1^+ \to 6_1^+)$ and the $B(E2; 6_1^+ \to 4_1^+)$ values are underestimated. The situation looks slightly better in ^{210}Po where the $B(E2; 4_1^+ \to 2_1^+)$ value is reproduced in SM1-gh calculations (see Table 6.3) while for ^{210}Pb this value is underestimated by a factor of 2 or more in both calculations (see Table 6.2). However, the results from the SM1-gh and SM2-gh clearly demonstrate that whatever the procedure for choosing the effective charges, the single-j shell model cannot provide a consistent description of the $B(E2)$ values for the yrast states of ^{210}Pb and ^{210}Po and, consequently, it cannot be expected that the same model will perform better at describing the $B(E2)$ values in ^{212}Po (cf. Table 6.1 and Fig. 6.1). Apparently, the key for understanding the structure of the low-lying yrast states in ^{212}Po which show unexpectedly low collectivity, lies in the understanding of the behaviour of the seniority-2 configurations in ^{210}Pb and ^{210}Po.

6.2 Realistic shell model calculations for ^{210}Po and ^{210}Pb

At this point, it can be speculated that the failure of the single-j shell model in the cases of ^{210}Po and ^{210}Pb originates from the severely limited model space. To check this hypothesis we have performed realistic shell-model calculations. The valence space consists of all neutron orbitals in the 126-184 shell ($3s_{1/2}$, $2d_{3/2}$, $2d_{5/2}$, $1g_{7/2}$, $1g_{9/2}$, $0h_{11/2}$ and $0j_{15/2}$) and all proton orbitals in the 82-126 shell

Table 6.3: Comparison between the experimental and calculated (see text for details) properties of the yrast states in ^{210}Po. The experimental excitation energies and $B(E2)$ values are from Ref. [57], unless otherwise specified.

J_i^π	E_x (MeV)		J_f^π	$B(E2; J_i \to J_f)(e^2\text{fm}^4)$			
	Expt	SM		Expt	SM1-gh^a	SM2-gh^b	SM^b
2_1^+	1.181	1.200	0_1^+	$136(21)^c$	263	137	133
4_1^+	1.427	1.466	2_1^+	$335(14)$	302	157	169
6_1^+	1.473	1.482	4_1^+	$229(7)$	209	109	116
8_1^+	1.557	1.533	6_1^+	$84(3)$	84	44	46

^{a}With $e_\pi = 1.52e$.
^{b}With $e_\pi = 1.09e$.
^{c}From the present work.

$(2p_{1/2}, 2p_{3/2}, 1f_{5/2}, 1f_{7/2}, 0h_{9/2},$ and $0i_{13/2})$. The Kuo-Herling interaction [76], which is an effective interaction tailored for this model space, is used to calculate properties of nuclei with two valence nucleons beyond ^{208}Pb. The single-particle energies are those given by Warburton and Brown [77]. The effective proton and neutron charges are the same as in the SM2-gh calculations. The results for both ^{210}Pb and ^{210}Po are presented in Tables 6.2 and 6.3, respectively, as well as in Fig. 6.2, labelled as SM.
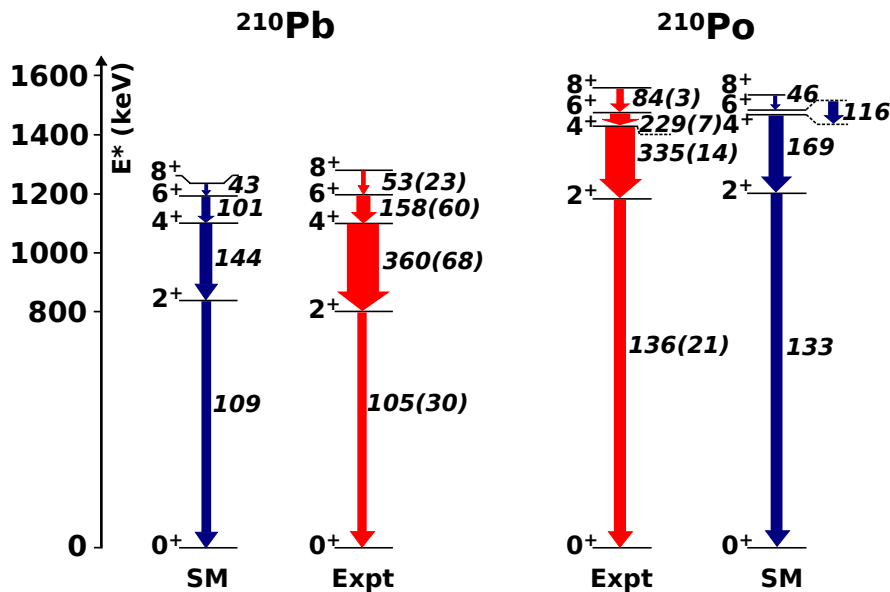

Figure 6.2: A graphical representation of the results from Tables 6.2 and 6.3 for realistic shell model calculations (SM) for the low-lying states in ^{210}Pb and ^{210}Po in comparison with experimental data (Expt). The thickness of the arrows is proportional to the $B(E2; 2_1^+ \to 0_1^+)$ values in $e^2\text{fm}^4$. The latter are also presented by the numbers next to the arrows.

The realistic shell-model (SM) reproduces almost perfectly the energies of the yrast states in ^{210}Pb and ^{210}Po (cf. Fig. 6.2). However, in both cases the descrip-

tion of the $B(E2)$ values is only marginally improved with respect to the ones obtained in the single-j shell-model calculation SM2-gh (cf. Tables 6.2 and 6.3). In this respect, it cannot be expected that realistic shell-model calculations will improve the description of the low-lying yrast states in ^{212}Po.

Chapter 7

Conclusion

In the present study, two experiments on low-energy quadrupole states of the nucleus ^{212}Po have been presented and their results have been discussed. By using data from an α-transfer reaction leading to ^{212}Po, we have measured the lifetimes of its first three 2^+ states. This was achieved by utilizing the DSA and RDDS methods. Both methods have been introduced and the techniques used for the analysis have been discussed. On the basis of extracted absolute $M1$ transition strength, it was shown that the 2_2^+ state in ^{212}Po is of predominantly isovector nature. **This represents the first identification of a low-lying isovector state in a nucleus from the mass $A \approx 208$ region.** The experimental data also reveals a weakened quadrupole collectivity in these non-yrast states which questions the applicability of the phonon picture in ^{212}Po. Instead, the data for the off-yrast states is qualitatively well described in the framework of a single-j empirical shell model which represents an extreme single-particle approximation. **All these findings indicate that the isovector nature of low-lying states is a property of the leading valence single-particle configuration.**

In addition, the extracted $B(E2; 2_1^+ \rightarrow 0_1^+)$ value shows also very low collectivity in the structure of the first excited 2^+ state in ^{212}Po. The low collectivity implies that appropriate theoretical understanding of the structure of the low-lying yrast states in ^{212}Po could be achieved within the framework of nuclear shell models. However, the performed shell-model calculations have shown that, while the energies of the states can be reproduced very well, no consistent description of the known $E2$ transition strengths in the yrast $2_1^+ - 4_1^+ - 6_1^+ - 8_1^+$ sequence could be obtained. **This problem appears to originate from the properties of the seniority-2 configurations in ^{210}Pb and ^{210}Po.**

In the course of this work, the lifetime of the 2_1^+ in ^{210}Po has been revised but the newly established value is still not high enough to resolve the puzzle observed in ^{212}Po. The performed QPM calculations which have been done for the nucleus ^{210}Po show that the problem existing in the shell model description also appears in a different form in the QPM calculations. **It is clear that the available microscopic models miss an essential part of the nuclear interaction when applied to describing the simplest excited nuclear states in the mass $A \approx 208$ region.** This situation prompts for a more thorough theoretical investigation of the low-energy structures of $A = 210$ isobars.

List of publications

The presented study is based on the following journal publications:

1. Original publications in peer-reviewed scientific journals

   • **_D. Kocheva_**, G. Rainovski, J. Jolie, N. Pietralla, A. Blazhev, R. Altenkirch, S. Ansari, A. Astier, M. Bast, M. Beckers, Th. Braunroth, M. Cappellazzo, A. Dewald, F. Diel, M. Djongolov, C. Fransen, K. Gladnishki, A. Goldkuhle, A. Hennig, V. Karayonchev, J.M. Keatings, E. Klug, Th. Kröll, J. Litzinger, K. Moschner, C. Müller-Gatermann, P. Petkov, M. Scheck, Ph. Scholz, T. Schmidt, P. Spagnoletti, C. Stahl, R. Stegmann, A. Stolz, A. Vogt, N. Warr, V. Werner, D. Wölk, J.C. Zamora, K.O. Zell, V.Yu. Ponomarev and P. Van Isacker;
   "Low collectivity of the 2_1^+ state of ^{212}Po"
   Physical Review C **96**, 044305 (2017); (IF 2016 - 3.820, 5-year 3.676)

   • **_D. Kocheva_**, G. Rainovski, J. Jolie, N. Pietralla, A. Blazhev, A. Astier, R. Altenkirch, S. Ansari, Th. Braunroth, M.L. Cortés, A. Dewald, F. Diel, M. Djongolov, C. Fransen, K. Gladnishki, A. Hennig, V. Karayonchev, J.M. Keatings, E. Kluge, J. Litzinger, C. Müller-Gatermann, P. Petkov, M. Rudigier, M. Scheck, Ph. Scholz, P. Spagnoletti, M. Spieker, C. Stahl, R. Stegmann, M. Stoyanova, P. Thöle, N. Warr, V. Werner, W. Witt, D. Wölk, K.O. Zell, P. Van Isacker and V.Yu. Ponomarev;
   "A revised B(E2;$2_1^+ \to 0_1^+$) value in the semi-magic nucleus ^{210}Po"
   European Physical Journal A **53**: 175 (2017); (IF 2016 - 2.833, 5-year 2.644)

   • **_D. Kocheva_**, G. Rainovski, J. Jolie, N. Pietralla, C. Stahl, P. Petkov, A. Blazhev, A. Hennig, A. Astier, Th. Braunroth, M.L. Cortés, A. Dewald, M. Djongolov, C. Fransen, K. Gladnishki, V. Karayonchev, J. Litzinger, C. Müller-Gatermann, M. Scheck, Ph. Scholz, R. Stegmann, P. Thöle, V. Werner, W. Witt, D. Wölk, P. Van Isacker;
   "Low-lying isovector 2^+ valence-shell excitations of ^{212}Po"
   Physical Review C **93**, 011303(R) (2016); (IF 2016 - 3.820, 5-year 3.676)

2. Conference proceedings

- **_D. Kocheva_**, G. Rainovski, J. Jolie, N. Pietralla, A. Blazhev, A. Astier, R. Altenkirch, M. Bast, M. Beckers, S. Ansari, Th. Braunroth, M. Cappellazzo, M.L. Cortés, A. Dewald, F. Diel, M. Djongolov, C. Fransen, K. Gladnishki, A. Goldkuhle, A. Hennig, V. Karayonchev, J.M. Keatings, E. Kluge, Th. Kröll, J. Litzinger, K. Moschner, C. Müller-Gatermann, P. Petkov, M. Rudigier, M. Scheck, P. Spagnoletti, Ph. Scholz, T. Schmidt, M. Spieker, C. Stahl, R. Stegmann, A. Stolz, A. Vogt, M. Stoyanova, P. Thöle, N. Warr, V. Werner, W. Witt, D. Wölk, J.C. Zamora, K.O. Zell, P. Van Isacker and V.Yu. Ponomarev;
"Low collectivity of the first 2^+ states of $^{210,212}Po$"
Journal of Physics: Conference Series, to be published;
XXII International School on Nuclear Physics and Applications

- **_D. Kocheva_**, G. Rainovski, J. Jolie, N. Pietralla, C. Stahl, P. Petkov, A. Blazhev, A. Hennig, A. Astier, Th. Braunroth, L. Cortes, A. Dewald, M. Djongolov, C. Fransen, K. Gladnishki, V. Karayonchev, J. Litzinger, C. Müller-Gatermann, M. Scheck, Ph. Scholz, C. Schramm, P. Thöle, V. Werner, W. Witt, D. Wölk and P. Van Isacker;
"Search for mixed-symmetry states in ^{212}Po"
Journal of Physics: Conference Series **724**, 012023 (2016);
XXI International School on Nuclear Physics, Neutron Physics and Applications

- **_D. Kocheva_**, R. Stegmann, G. Rainovski, J. Jolie, N. Pietralla, C. Stahl, P. Petkov, A. Blazhev, A. Hennig, C. Bauer, Th. Braunroth, M.P. Carpenter, L. Cortes, A. Dewald, M. Djongolov, C. Fransen, K. Gladnishki, R.V. F. Janssens, V. Karayonchev, M. Lettmann, C.J. Lister, J. Litzinger, Th. Möller, C. Müller-Gatermann, M. Scheck, Ph. Scholz, C. Schramm, P. Thöle, V. Werner, D. Wölk, S. Zhu and P. Van Isacker;
"Search for mixed-symmetry states of nuclei in the vicinity of the double-magic nucleus ^{208}Pb"
EPJ Web of Conferences **107**, 03004 (2016);
International Conference on Nuclear Structure and Related Topics (NSRT15)

Other publications of the author:

• T. Konstantinopoulos T. Konstantinopoulos, P. Petkov, A. Goasduff, T. Arici, A. Astier, L. Atanasova, M. Axiotis, D. Bonatsos, P. Detistov, A. Dewald, M. J. Eller, V. Foteinou, A. Gargano, G. Georgiev, K. Gladnishki, A. Gottardo, S. Harissopulos, H. Hess, S. Kaim, ***<u>D. Kocheva</u>***, A. Kusoglu, A. Lagoyannis, J. Ljungvall, R. Lutter, I. Matea, B. Melon, T. J. Mertzimekis, A. Nannini, C. M. Petrache, A. Petrovici, G. Provatas, P. Reiter, M. Rocchini, S. Roccia, M. Seidlitz, B. Siebeck, D. Suzuki, N. Warr, H. De Witte and T. Zerrouki;
"Lifetime measurements in ^{100}Ru"
Physical Review C **95**, 014309 (2017);

• D. Ralet, G. Georgiev, A. E. Stuchbery, E. Clément, A. Lemasson, C. Michelagnoli, M. Rejmund, L. Atanasova, D. L. Balabanski, G. Bocchi, R. Carroll, A. Dewald, J. Dudouet, B. Fornal, G. de France, S. Franchoo, C. Fransen, C. Müller-Gatermann, A. Goasduff, A. Gadea, B. Jacquot, P. R. John, ***<u>D. Kocheva</u>***, T. Konstantinopoulos, A. Korichi, A. Kusoglu, S. M. Lenzi, S. Leoni, J. Ljungvall, R. Lozeva, A. Maj, A. Navin, R. Perez, N. Pietralla, C. Shand, O. Stezowski and D. Yordanov;
"Toward lifetime and g factor measurements of short-lived states in the vicinity of ^{208}Pb"
Physica Scripta **92**, 054004 (2017);

Acknowledgements

I would like to thank my supervisor Prof. Dr. Georgi Rainovski for the support he has given me during my entire education. I want to thank him for the opportunity of working on this thesis, for always being open for questions and discussions, and providing valuable ideas on numerous issues of the analyses and their interpretation. I would like to thank him for the patience and for having confidence in me during all these years.

I want to thank Dr. Martin Djongolov and Dr. Kalin Gladnishki for various discussions related to the nuclear physics and for suggestions regarding issues which appeared during the data analysis.

I would like to thank Prof. Dr. Norbert Pietralla for the opportunity of working five months at TU Darmstadt. I want to thank him, Dr. Volker Werner and Dr. Christian Stahl for the useful ideas related to the analysis of our experimental data. I want to thank Dr. V. Yu. Ponomarev for taking time for me and being open for questions during my stay at TU Darmstadt. I also want to thank him for performing the theoretical calculations based on the quasiparticle phonon model.

Bibliography

[1] R. F. Casten, *Nuclear Structure from Simple Perspective*, Oxford: Oxford University Press (2000).

[2] National Nuclear Data Center. *Information extracted from the Chart of Nuclides database.* http://www.nndc.bnl.gov/chart/, visited January 26th, 2018.

[3] M. G. Mayer, Phys. Rev. **75**, 1969 (1949).

[4] O. Haxel; J. H. D. Jensen; H. E. Suess, Phys. Rev. **75**, 1766 (1949).

[5] A. Bohr & B. R. Mottelson, *Nuclear structure, Volume II: Nuclear Deformations*, Advanced Book Program Reading, Massachusetts (1975).

[6] F. Iachello and A. Arima, *The interacting boson model*, Cambridge: Cambridge University Press (1987).

[7] G. Racah, Phys. Rev. **63**, (1943) 367.

[8] J. J. Ressler *et al.*, Phys. Rev. C **69**, 034331 (2004).

[9] N. Auerbach, I. Talmi, Phys. Lett. **10**, 297 (1964).

[10] R.M. Lieder *et al.*, Phys. Rev. Lett. **41**, 742 (1978); P.A. Baidsen *et al.*, Phys. Rev. Lett. **41**, 738 (1978); P. Lemmertz *et al.*, Z. Phys. A **298**, 311 (1980).

[11] A.R. Poletti *et al.*, Nucl. Phys. A **473**, 595 (1987).

[12] E. Browne, Nucl. Data Sheets **104**, 427 (2005).

[13] J. D. Holt, N. Pietralla, J. W. Holt, T. T. S. Kuo, and G. Rainovski, Phys. Rev. C **76**, 034325 (2007)

[14] T. Togashi *et al.*, Phys. Rev. Letters **117**, 172502 (2016).

[15] N. Pietralla, P. von Brentano, A. F. Lisetskiy, Prog. Part. Nucl. Phys. **60**, 225 (2008).

[16] G. Rainovski *et al.*, Phys. Rev. Lett. **96**, 122501 (2006).

[17] T. Ahn *et al.*, Phys. Lett. B **679**, 19 (2009).

[18] L. Coquard *et al.*, Phys. Rev. C **82**, 024317 (2010).

[19] K.A. Gladnishki *et al.*, Phys. Rev. C **82**, 037302 (2010).

[20] M. Danchev *et al.*, Phys. Rev. C **84**, 061306(R) (2011).

[21] T. Ahn *et al.*, Phys. Rev. C **86**, 014303 (2012).

[22] A. Astier, P. Petkov, M.-G. Porquet, D.S. Delion, and P. Schuck, Phys. Rev. Lett. **104**, 042701 (2010); A. Astier, P. Petkov, M.-G. Porquet, D.S. Delion, and P. Schuck, Eur. Phys. J. A **46**, 165 (2010).

[23] B. Bengtson *et al.*, Nucl. Phys. A **378**, 1 (1982).

[24] K. Heyde, P. von Neumann-Cosel, A. Richter, Rev. Mod. Phys. **82**, 2366 (2010).

[25] G. Rainovski, Dissertation for acquiring the scientific degree of doctor of the physical sciences, University of Sofia St. Kliment Ohridski (2012).

[26] J.J. Ressler *et al.*, Phys. Rev. C **69**, 034317 (2004).

[27] T. Grahn *et al.*, Eur. Phys. J. A **52**, 340 (2016).

[28] N. Lo Iudice and F. Palumbo, Phys. Rev. Lett. **41**, 1532 (1978)

[29] F. Iachello, Phys. Rev. Lett. **53**, 1427 (1984).

[30] M.G. Mayer and J.H.D. Jensen,*Elementary Theory of Nuclear Shell Structure* (John Wiley & Sons, Inc., (1955).

[31] A. Arima *et al.*, Phys. Lett. B **66**, 205 (1977).

[32] T. Otsuka *et al.*, Phys. Lett. B **76**, 139 (1978).

[33] D. Bohle *et al.*, Phys. Lett. B **137**, 27 (1984).

[34] P. Van Isacker et al., Ann. Phys. (NY) **171**, 253 (1986).

[35] T.K. Alexander and J.S. Forster, Adv. Nucl. Phys. **10**, 197 (1978).

[36] A. E. Blaugrund, Nucl. Phys. **88**, 5001-512 (1966).

[37] B. Melon, PhD thesis, Universität zu Köln (2011).

[38] A. Dewald, O. Möller, P. Petkov, Prog. Part. Nucl. Phys. **67**, 786 (2012).

[39] Zs. Podolýak *et al.*, Nucl. Instrum. Methods Phys. Res. A **511**, 354 (2003).

[40] A.B. Garnsworthy *et al.*, J. Phys. G **31**, S1851 (2005).

[41] O. Tarasov, D. Bazin, Nucl. Instr. Meth. B **266**, 4657 (2008)

[42] D. Bazin et al., Nucl. Instr. Meth. A **482**, 307 (2002)

78

[43] J. Lindhard, M. Scharff, and H.E. Schiøtt, Kgl. Dan. Vid. Selsk. Mat. Fys. Medd. **33**, 14 (1963).

[44] A. Anttila, M. Bister, and J. Keinonen, Z. Phys. **A274**:227 (1975).

[45] M. Bister, A. Anttila, and J. Keinonen, Phys. Lett. **53A**:471 (1975).

[46] K. G. Shane, H. Laumer, and G. G. Seaman, J. Appl. Phys. **47**:2286 (1976).

[47] P. Petkov *et al.*, Nucl. Phys. A **640**, 293 (1998).

[48] P. Petkov *et al.*, Nucl. Instrum. Methods Phys. Res. A **431**, 208 (1999).

[49] G. Winter, ZfK. Rossendorf Report ZfK-497, 1983; G. Winter, Nucl. Instrum. Methods **214**, 537 (1983).

[50] L.C. Northcliffe and R.F. Schilling, Nucl. Data Sect. **7**, 233 (1970).

[51] J.F. Ziegler and J.P. Biersack, in *Treatise on Heavy Ion Science*, edited by D.A. Bromley (Plenum Press, New York, 1985), Vol. 6, p. 95.

[52] J. Keinonen, AIP Conf. Proc. **125**, 557 (1985).

[53] C. Stahl, J. Leske, M. Lettmann, N. Pietralla, Comp. Phys. Com. **214**, (2017) 174.

[54] C. Stahl, PhD thesis, TU Darmstadt (2015).

[55] S. Agostinelli *et al.*, Nucl. Instrum. Methods Phys. Res. A **506**, 250 (2003).

[56] J.F. Ziegler, M.D. Ziegler, J.P. Biersack, Nucl. Instr Meth., B **268**, 1823 (2010).

[57] M. Shamsuzzoha Basunia, Nucl. Data Sheets **121**, 561 (2014).

[58] A.P. Yutsis, I.B. Levinson and V.V. Vanagas, The Theory of Angular Momentum (Israel Program for Scientific Translations, Jerusalem, 1962).

[59] J. Chen and F.G. Kondev, Nucl. Data Sheets **126**, 373 (2015).

[60] A.Z. Schwarzschild, E.K. Warburton, Ann. Rev. Nucl. Sci. **18**, 265 (1968).

[61] A. Dewald, S. Harissopulos and P. von Brentano, Z. Phys. A**334**, 163 (1989).

[62] G. Böhm, A. Dewald, P. Petkov and P. von Brentano, Nucl. Inst. Meth. A **329**, 248 (1993).

[63] C. Ellegaard *et al.*, Nucl. Phys. A **206**, (1973) 83.

[64] L. Coraggio *et al.*, Phys. Rev. C **60**, (1999) 064306.

[65] E. Caurier, M. Rejmund, H. Grawe, Phys. Rev. C **67**, (2003) 054310.

[66] L. G. Mann *et al.*, Phys. Rev. C **38**, (1988) 74.

[67] O. Häusser *et al.*, Nucl. Phys. A **273**, (1976) 253.

[68] A.E. Stuchbery, AIP Conference Proceedings **1625**, (2014) 52.

[69] F. Nowacki, Nucl. Phys. **A704**, (2002) 223.

[70] V. G. Soloviev, Theory of Atomic Nuclei, Quasiparticles and Phonons (IOP, London, 1992).

[71] N.Lo Iudice *et al.*, Journal of Phys. G **39** (2012), 043101.

[72] R. Stegmann, PhD thesis, TU Darmstadt (2017).

[73] C.A. Bertulani and V.Yu. Ponomarev, Phys. Rep. **321**, (1999) 139.

[74] V.V. Voronov and Dao Tien Khoa, Izv. AN SSSR, ser. fiz., **48**, (1984) 2008.

[75] V.Yu. Ponomarev, Ch. Stoyanov, N. Tsoneva, and M. Grinberg, Nucl. Phys. **A635**, (1998) 470.

[76] G.H. Herling and T.T.S. Kuo, Nucl. Phys. A **181**, 113 (1979).

[77] E. K. Warburton and B. A. Brown, Phys. Rev. C **43**, (1991) 602.